

RL-TR-97-94
Final Technical Report
September 1997



MAXIMUM LIKELIHOOD ADAPTIVE NEURAL SYSTEMS (MLANS) APPLICATION TO HIGH FREQUENCY (HF) PROPAGATION

Nichols Research Corp.

L.I. Perlovsky, T.C. Marzetta, V.H. Webb, and C.P. Plum

APPROVED FOR PUBLIC RELEASE; DISTRIBUTION UNLIMITED.

19980310 147

DTIC QUALITY INSPECTED 4

**Rome Laboratory
Air Force Materiel Command
Rome, New York**

Although this report references limited document (*), listed on page 36, no limited information has been extracted.

This report has been reviewed by the Rome Laboratory Public Affairs Office (PA) and is releasable to the National Technical Information Service (NTIS). At NTIS it will be releasable to the general public, including foreign nations.

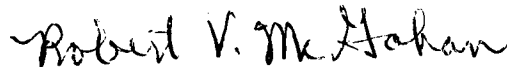
RL-TR-97-94 has been reviewed and is approved for publication.

APPROVED:



BERTUS WEIJERS
Project Engineer

FOR THE DIRECTOR:



ROBERT V. MCGAHAN, Acting Director
Electromagnetics and Reliability Directorate

If your address has changed or if you wish to be removed from the Rome Laboratory mailing list, or if the addressee is no longer employed by your organization, please notify RL/ERCP, 31 Grenier St., Hanscom AFB MA 01731-3010. This will assist us in maintaining a current mailing list.

Do not return copies of this report unless contractual obligations or notices on a specific document require that it be returned.

REPORT DOCUMENTATION PAGE			Form Approved OMB No. 0704-0188	
Public reporting burden for this collection of information is estimated to average 1 hour per response, including the time for reviewing instructions, searching existing data sources, gathering and maintaining the data needed, and completing and reviewing the collection of information. Send comments regarding this burden estimate or any other aspect of this collection of information, including suggestions for reducing this burden, to Washington Headquarters Services, Directorate for Information Operations and Reports, 1215 Jefferson Davis Highway, Suite 1204, Arlington, VA 22202-4302, and to the Office of Management and Budget, Paperwork Reduction Project (0704-0188), Washington, DC 20503.				
1. AGENCY USE ONLY (Leave blank)	2. REPORT DATE Sep 97	3. REPORT TYPE AND DATES COVERED Final Apr 94 - Dec 94		
4. TITLE AND SUBTITLE MAXIMUM LIKELIHOOD ADAPTIVE NEURAL SYSTEM (MLANS) APPLICATION TO HIGH FREQUENCY (HF) PROPAGATION		5. FUNDING NUMBERS C - F19628-94-C-0049 PE - 62702F PR - 4600 TA - 16 WU -89		
6. AUTHOR(S) L.I. Perlovsky, T.L. Marzetta, V.H. Webb, and C.P. Plum				
7. PERFORMING ORGANIZATION NAME(S) AND ADDRESS(ES) Nichols Research Corporation 251 Edgewater Drive Wakefield, MA 01880		8. PERFORMING ORGANIZATION REPORT NUMBER NRC-TR-94-149		
9. SPONSORING/MONITORING AGENCY NAME(S) AND ADDRESS(ES) Rome Laboratory 31 Grenier Street Hanscom AFB MA 01731-3010		10. SPONSORING/MONITORING AGENCY REPORT NUMBER RL-TR-97-94		
11. SUPPLEMENTARY NOTES Rome Laboratory Project Engineer: Bertus Weijers/ERCP/478-2527				
12a. DISTRIBUTION AVAILABILITY STATEMENT Approved for Public Release; Distribution Unlimited.		12b. DISTRIBUTION CODE		
13. ABSTRACT (Maximum 200 words) The feasibility of applying a model-based neural network technique to investigate the properties of ionospheric clutter observed in the operation of high frequency (HF) propagation systems was examined. Individual ionospheric clutter structures found in the amplitude-range-Doppler (ARD) spectra of over-the-horizon (OTH) radar data were successfully segmented and characterized. A multi-mode Gaussian clutter model was formulated using the Maximum Likelihood Adaptive Neural System (MLANS) to fit the observations. The results indicate that either a three-or a four-mode Gaussian model is sufficient for MLANS to segment and characterize the observed clutter. High-Fidelity simulations of time slices of the raw data were achieved by combining time-varying Gaussians together with a time-varying uniform distribution to represent the noise floor. Each Gaussian mode (or model) is characterized by a time-varying set of three parameters: amplitude, Doppler spread, and Doppler shift.				
14. SUBJECT TERMS Neural Networks, Ionospheric Clutter, Over-The-Horizon Radar, HF Radar, HF Propagation, Clutter Segmentation, MLANS		15. NUMBER OF PAGES 72		
		16. PRICE CODE		
17. SECURITY CLASSIFICATION OF REPORT UNCLASSIFIED	18. SECURITY CLASSIFICATION OF THIS PAGE UNCLASSIFIED	19. SECURITY CLASSIFICATION OF ABSTRACT UNCLASSIFIED	20. LIMITATION OF ABSTRACT UL	

TABLE OF CONTENTS

	<u>PAGE</u>
LIST OF ILLUSTRATIONS	ii
LIST OF ACRONYMS.....	iv
ACKNOWLEDGEMENTS.....	v
EXECUTIVE SUMMARY	vi
 SECTION 1. INTRODUCTION.....	 1
 SECTION 2. MLANS BACKGROUND AND FORMULATION.....	 3
2.1 <u>BACKGROUND</u>	3
2.2 <u>MLANS PARAMETRIC REPRESENTATION OF HF RADAR</u> <u>DOPPLER SPECTRA</u>	6
 SECTION 3. RESULTS AND DISCUSSION.....	 13
3.1 <u>REPRESENTATIVE HF RADAR DATA</u>	13
3.2 <u>CLUTTER SEGMENTATION RESULTS</u>	16
3.2.1 <u>3-Mode Gaussian Clutter Model</u>	17
3.2.2 <u>4-Mode Gaussian Clutter Model</u>	21
3.2.3 <u>Model Parameter Functionality</u>	24
3.2.4 <u>Fits to Averaged Data</u>	29
 SECTION 4. CONCLUSIONS	 34
 SECTION 5. RECOMMENDATIONS.....	 35
 REFERENCES	 36
 APPENDIX A. CONVERGENCE OF MLANS EM.....	 A-1
 APPENDIX B. APPLICATION TO SIMULTANEOUS DETECTION AND TRACKING	 B-1
 APPENDIX C. ASSESSMENT OF THE APPLICABILITY OF THE HYPERBOLIC FILTER TO HF RADAR TARGET DETECTION.....	 C-1

LIST OF ILLUSTRATIONS

		<u>Page</u>
Figure 1.	MLANS Application to Modeling HF Doppler Spectra	12
Figure 2.	Sample HF Radar Doppler Spectra Data Set.....	13
Figure 3.	Representative Radar Doppler Spectrum	16
Figure 4.	Three-Mode Gaussian Model Fits for Spectrum Numbers 6-9, B34, RB1 Data Set. A Single Uniform Model is Also Included	18
Figure 5.	Three-Mode Gaussian Model Fits for Spectrum Numbers 91-94, B34, RB1 Data Set. A Single Uniform Model is Also Included	19
Figure 6.	Artist's Sketch of the Radar Beam Propagation with Multiple Hops	20
Figure 7.	Consolidated Three-Mode Gaussian Model Fits and Raw Image Data for B34, RB1 Data Set	21
Figure 8.	Four-Mode Gaussian Model Fits for Spectrum Numbers 6-9, B34, RB1 Data Set	22
Figure 9.	Four-Mode Gaussian Model Fits for Spectrum Numbers 91-94, B34, RB1 Data Set	23
Figure 10.	Consolidated Four-Mode Gaussian Model Fits and Raw Image Data for B34, RB1 Data Set	24
Figure 11.	Plot of the Center Frequencies for the Three-Mode Gaussian Model as Compared to the Raw Image Data for B34, RB1 Data Set.....	25
Figure 12.	Plot of the Center Frequencies for the Four-Mode Gaussian Model as Compared to the Raw Image Data for B34, RB1 Data Set.....	26
Figure 13.	Plot of the Gaussian Mode Amplitudes for B34, RB1 Data Set.....	27
Figure 14.	Plot of the Gaussian Mode Variances for B34, RB1 Data Set Black Bands at Top Indicate Periods of Operator Intervention	27
Figure 15.	Consolidated Three-Mode Gaussian Model Fit and Raw Image Data for B34, RB9 Data Set. Also Shown Superimposed on the Raw Image Plot are the Center Frequencies for the Three-Mode Gaussian Model	28
Figure 16.	Consolidated Three-Mode Gaussian Model Fit and Raw Image Data for B36, RB1 Data Set. Also Shown Superimposed on the Raw Image Plot are the Center Frequencies for the Three-Mode Gaussian Model	29
Figure 17.	Three-Mode Gaussian Model Fits for Average of Spectrum Numbers 6, 7, and 8, B34, RB1	30

LIST OF ILLUSTRATIONS (Concluded)

	<u>Page</u>
Figure 18. Three-Mode Gaussian Model Fits for Average of Spectrum Numbers 92, 93 and 94, B34, RB1	31
Figure 19. Consolidated Three-Mode Gaussian Model Fit and Raw Image Data for Three Spectrum Average of the B34, RB1 Data Set. Also Plotted on the Left Side are the Center Frequencies for the Three-Mode Gaussian Model	32
Figure 20. Plot of the Gaussian Mode Amplitudes for the Three Spectrum Average of the B34, RB1 Data Set	33
Figure 21. Plot of the Gaussian Mode Variances for the Three Spectrum Average of the B34, RB1 Data Set. Black Bands at Top Indicate Periods of Operator Intervention	33

LIST OF ACRONYMS

CIT	Coherent Integration Time
dB	Decibels
DoD	Department of Defense
E	Expectation
ECRS	East Coast Radar System
EM	Expectation-Maximization
HF	High Frequency
JPDA	Joint Probability Density Association
km	Kilometer
L	Likelihood
LL	Log Likelihood
M	Maximization
MAP	Maximum A-Posteriori
MHT	Multiple Hypothesis Tracking
ML	Maximum Likelihood
MLANS	Maximum Likelihood Adaptive Neural System
nm	Nautical Mile
NRC	Nichols Research Corporation
OTH	Over the Horizon
OTH-B	Over the Horizon Backscatter
pdf	Probability Distribution Function
RB	Range Bin
SR	Start Range
UT	Universal Time
WRF	Waveform Repetition Frequency

ACKNOWLEDGMENTS

The authors acknowledge and express their appreciation to the following Rome Laboratory engineers and scientists who contributed to this document:

Elihu J. Tichovolsky

Bertus Weijers

David Choi

Peter R. Franchi

The authors acknowledge the guidance and assistance of Bert Weijers, RL/ERCPC, the Contracting Officer's Technical Representative.

EXECUTIVE SUMMARY

This report presents the results of a research effort to examine the feasibility of applying a model-based neural network technique to investigate the properties of ionospheric clutter observed in the operation of high frequency (HF) propagation systems. The primary objective of this initial phase of the supporting contract was to demonstrate the capability to characterize and segment ionospheric clutter structures observed during operation of an HF radar system. Clutter observed in the operation of systems that use the ionosphere as a refractive medium can be intense, adversely affecting system performance. Understanding the spatial and temporal dependence of ionospheric clutter could lead to methods to mitigate against the clutter, leading to improved system performance.

The primary analysis tool used in this study was the Maximum Likelihood Adaptive Neural System (MLANS), a new and innovative algorithm analysis technique which implements a model-based, statistical algorithm approach in a neural-network environment. By parameterizing the large number of neural-network weights in terms of the relatively small number of model parameters, MLANS utilizes all available information and is fast and efficient for complicated real-world problems, such as those associated with the operation of HF systems. The data used for this research effort is from the over-the-horizon (OTH) HF radar system developed and operated by the United States Air Force in the state of Maine.

For this initial study phase, a multi-mode Gaussian clutter model was used to fit the observed HF radar Doppler spectra. The mathematical formulation for the multi-mode Gaussian model is presented and discussed, along with a description of the implementation within MLANS. A uniform clutter model is included in the formulation to describe the background clutter, which is caused by such phenomena as meteors transiting the ionosphere, magnetic field aligned ionospheric irregularities, and lightning events. The essence of MLANS is to perform Bayesian inference based on a mixture-density model. The complete probabilistic model is described by the prior class probabilities, and by the class-conditional probability density for the measurements. The mixture-density formulation is highly flexible and is capable of modeling non-Gaussian behavior.

Key study results are that the MLANS neural network is able to both characterize and segment the observed ionospheric clutter using both three- and four-mode Gaussian clutter

models in combination with a uniform model. A formulation is also presented for applying the MLANS algorithm to enhance the detection and tracking performance of HF radar systems, especially in the regions of strong ionospheric clutter. Recommendations are made regarding the use of the MLANS neural network to perform a detailed analysis of equatorial ionospheric clutter using both a Gaussian model and a power law model formulation and to investigate the application of MLANS as a simultaneous detection and tracking signal processing algorithm.

SECTION 1. INTRODUCTION

This report describes the results of a research effort in applying a novel and innovative neural-network algorithmic technique to investigate the properties of ionospheric clutter observed in the operation of high frequency (HF) propagation systems. This work is supported by Rome Laboratory and in part by the Electronic Systems Center, Surveillance and Control Systems Program Office under Contract Number F19628-94-C-0049. The primary objective of this initial phase of this contract was to demonstrate the capability to characterize and segment ionospheric clutter structures observed during operation of an HF radar system.

The primary analysis tool used in this study was the Maximum Likelihood Adaptive Neural System (MLANS), a new and innovative algorithm analysis technique which implements a model-based, statistical algorithm approach in a neural-network environment. By parameterizing the large number of neural-network weights in terms of the relatively small number of model parameters, MLANS utilizes all available information and is fast and efficient for complicated real-world problems, such as those associated with the operation of HF systems. The data used for this research effort is from the over-the-horizon backscatter (OTH-B) HF radar system developed and operated by the United States Air Force in the state of Maine. This system is termed the East Coast Radar System (ECRS).

The MLANS neural network was developed by NRC under previous Department of Defense (DoD) contract sponsorship. It is being evaluated in many DoD application areas such as warhead discrimination, sensor fusion, detection and tracking in high clutter, strategic and tactical automatic target cueing/recognition, and underwater target detection, tracking, and classification. In these applications, MLANS has been applied to many sensor systems, including radar, electro-optical, laser, and acoustic. MLANS has been found to be a powerful analysis tool, offering a novel solution to many complicated, real-world problems due to its capability of estimating parameters of physical and statistical models concurrently with separation of signals into modes corresponding to various physical sources. It is envisioned that the MLANS neural network will be equally successful and valuable as a research tool for investigating the propagation phenomena associated with the operation of OTH radars and other HF systems, potentially leading to improving the operational performance of such systems.

It is important to note that the objective of this initial research effort under the sponsoring contract was solely to demonstrate the *feasibility* of using the MLANS neural network to characterize and segment the ionospheric clutter observed in the operation of a HF radar system. We were not concerned during this phase of the study with such physical phenomena, for example, as investigating the specific propagation mode through the ionosphere for the HF beam, for investigating the specific properties of ionospheric clutter, nor for performing a full study of MLANS' simultaneous detecting and tracking capability for HF radar systems. These and other topics are potential subjects for further study under the sponsoring contract.

The next section contains a discussion on the background of MLANS, and presents the mathematical formulation of MLANS with a multi-modal Gaussian clutter model plus a uniform clutter model. Section 3 then contains the results of the research for both clutter characterization and segmentation. Section 4 presents the study conclusions and Section 5 presents our recommendations for further study.

SECTION 2. MLANS BACKGROUND AND FORMULATION

2.1 BACKGROUND

A vast array of neural-network approaches are available for potential application to HF systems for such functions as modeling, estimation, tracking, and decision. These approaches include back propagation, adaptive resonance theory, the Hopfield net, reduced Coulomb energy, the Kohonen net, and others [1]. However each of these approaches has major difficulties, including slow learning and the requirement for large training data sets. MLANS combines model-based statistical and neural-network approaches. By parameterizing the large number of neural-network weights in terms of a small number of model parameters, it utilizes all available information and it is fast and efficient for complicated real-world problems. In effect MLANS is a "smart" neural network.

The MLANS neural network has a novel architecture: it does not have hidden layers, still it is capable of designing classifiers of arbitrarily complex shapes by utilizing structured maximum likelihood (ML) neurons. MLANS weights are a-posteriori probabilities making MLANS well suited for classification (i.e., the probability of belonging to a specific class or type), as well as to other problems such as data fusion (i.e., probabilities calculated from different data sources are readily combined), and tracking (i.e., track assignment, frame-to-frame correlation, and sensor correlation with other data sources are functions driven by probabilistic associations). MLANS is a model-based parametric neural network. This means that the weights are functions of a relatively few parameters. These parameters can be determined quickly resulting in a rapid learning speed. MLANS performance has been shown to achieve the Cramer-Rao bound on learning speed [2].

MLANS was first introduced by Perlovsky in 1987 [3]. The general architecture of MLANS has been previously described in the open literature [2]. A key facet of this neural network is the building of an internal model of objects (or of physical processes). These models can have statistical, geometric, and dynamic aspects, and they can incorporate elements of self-learning of symbolic representations. An overview explanation of MLANS follows.

The essence of MLANS is to perform Bayesian inference based on a mixture-density model. Let $\{X_1, \dots, X_N\}$ be a set of N measurements, possibly vector-valued. MLANS models their joint probability density in the form

$$p(X_1, \dots, X_N) = \sum_{C_1=1}^M \dots \sum_{C_N=1}^M p(X_1, \dots, X_N | C_1, \dots, C_N) \cdot p(C_1, \dots, C_N), \quad (1)$$

where C_n is the mode membership of the n -th observation, X_n .

The complete probabilistic model is described by the prior class probabilities and by the class-conditional probability density for the measurements. The mixture-density formulation is highly flexible and is capable of modeling non-Gaussian behavior.

The mixture-density model can be used in several different ways. One application is to assign the measurements to their class membership. An application of Bayes' rule gives the joint a-posteriori class-membership probability,

$$p(C_1, \dots, C_N | X_1, \dots, X_N) = \frac{p(X_1, \dots, X_N | C_1, \dots, C_N) \cdot p(C_1, \dots, C_N)}{p(X_1, \dots, X_N)}, \quad (2)$$

which represents the most complete information about the class-membership that can be inferred from the measurements and models of targets and clutter. Generally the maximum a-posteriori (MAP) class assignments are of greatest interest, obtained by choosing the class memberships jointly to maximize the a-posteriori likelihood.

One approach to target detection is to use a likelihood ratio test between target and clutter over some set of measurements:

$$p(X_1, \dots, X_N | \text{target}) + p(X_1, \dots, X_N | \text{clutter}) \underset{\text{clutter}}{\overset{\text{target}}{>}} \eta, \quad (3)$$

where the target- and clutter-dependent probability densities are mixture densities and η is a threshold chosen to give the desired detection and false-alarm probabilities.

The MLANS structure can handle a variety of models for the class-conditional probability densities of the measurements and for the prior class probabilities. Gaussian, uniform, Raleigh, log-normal, and Rician class-conditional probability densities have been used in previous work. It

is also feasible (and sometimes necessary) to represent the class-conditional probability densities themselves as mixture densities.

For many applications of MLANS it is reasonable to model the class-memberships as statistically independent,

$$p(C_1, \dots, C_N) = p(C_1) \dots p(C_N), \quad (4)$$

and the measurements as conditionally statistically independent,

$$p(X_1, \dots, X_N | C_1, \dots, C_N) = p(X_1 | C_1) \dots p(X_N | C_N). \quad (5)$$

As a result the measurements are unconditionally statistically independent, and the class-memberships are conditionally statistically independent. Note that the measurements themselves may be vectors, and statistical dependencies between the components of the measurement vector are still modeled by the class-conditional probability density.

Deterministic dependencies between measurements are incorporated by using appropriate models. For example, target and clutter movement is modeled by tracking models, which relate the center frequency positions of the corresponding modes in time, range, angle, and Doppler. These models can be simple models of linear motion, and can include acceleration terms or more complicated diurnal variation models.

The parameters that characterize the mixture density model generally have to be estimated from a set of data. In non-adaptive applications of MLANS, the parameters are estimated from training data. Alternatively, the parameters can be estimated adaptively from the data set about which Bayesian inferences are to be made. For either non-adaptive or adaptive parameter estimation, MLANS uses ML estimation: the parameters characterizing the mixture density are chosen to maximize the joint likelihood of the observed data. For mixture densities, a direct maximization is not feasible, i.e., setting derivatives of the log-likelihood to zero results in an intractable set of coupled nonlinear equations. For that reason, MLANS uses the EM (expectation-maximization) algorithm of Dempster et al [4], an iterative algorithm. The EM algorithm is "safe" in the sense that the likelihood at each iteration is guaranteed to increase. Various types of prior

and auxiliary information can be incorporated within the EM algorithm. For example, both deterministic and probabilistic information concerning class-memberships of some or all of the measurements can be handled by means of "teacher" probabilities.

MLANS is thus a very powerful, general tool for modeling and for statistical inference. The main objective of this research effort is to demonstrate that MLANS can be used as a research tool to help segment ionospheric clutter observed in the operation of HF systems. Through this process, specific properties of the ionospheric clutter model parameters can be identified and thus investigated. The next section describes a very specific and focused application of MLANS to the problem of finding a parametric representation of a measured HF radar Doppler spectrum as applied herein for this research study.

2.2 MLANS PARAMETRIC REPRESENTATION OF HF RADAR DOPPLER SPECTRA

Given a measured Doppler spectrum at N discrete frequencies, $\{S(\omega_n), 1 \leq n \leq N\}$, the object is to find a parsimonious representation for the spectrum, $\hat{S}(\omega_n)$, such that

$$S(\omega_n) \approx \hat{S}(\omega_n), \quad 1 \leq n \leq N. \quad (6)$$

In terms of a set of M basis functions or models,

$$\hat{S}(\omega) = \sum_{m=1}^M A_m \cdot F(\omega|m). \quad (7)$$

The idea is to choose the amplitudes, A_m , and parameters of models $F(\omega|m)$ so that the overall spectrum model, i.e., the right-hand side of Equation (6), best matches the measured spectrum, i.e., the left-hand side of Equation (6), according to the ML principle. The basis functions used in the spectral model are non negative-valued, and generally overlapping in frequency (so, non-orthogonal) which makes the problem of directly finding the best-fit parameters a difficult one, since the parameters for the different basis functions cannot be adjusted independently. MLANS circumvents this difficulty by using a clever iterative scheme which, at each iteration, involves independently fitting each of the basis functions to a weighted set of measurements.

The MLANS algorithm can estimate models comprising any combination of different types of basis functions. The current research emphasizes two types of basis functions: uniform and Gaussian:

$$\text{Uniform} \quad m=1, \quad F(\omega|m) = \frac{1}{W}, \quad -\frac{W}{2} < \omega < \frac{W}{2} \quad (8)$$

$$\text{Gaussian} \quad m=2, \dots, M, \quad F(\omega|m) = \frac{1}{\sqrt{2\pi} \Delta\omega_m} \exp\{-0.5(\omega - \bar{\omega}_m)^2 / \Delta\omega_m^2\}. \quad (9)$$

The basis functions are normalized to have unit area. The parameters characterizing the Gaussian basis functions are the mean or central frequency, $\bar{\omega}_m$, and the variance, $\Delta\omega_m$. The uniform model parameter, W , is taken to be the overall width of the Doppler frequency spectrum. The Gaussian model for HF radar clutter is asserted to be due to phase screen modulation as described by Franchi and Tichovolsky [5].

The ML estimation equations are derived utilizing Einstein's concept of a spectrum being a probability distribution function (pdf) for the photon distribution of likelihood L ,

$$L = \prod_p \text{pdf}(p) = \prod_p \hat{S}(\omega_p), \quad (10)$$

where here p is a photon number, and ω_p is the photon frequency. This can be written by combining terms for photons of identical frequencies. The number of photons with frequency ω is

$$NP(\omega) = S(\omega) / \omega\hbar, \quad (11)$$

so that Equation (10) can be written as

$$L = \prod_{\omega} \prod_{p|\omega} \hat{S}(\omega) = \prod_{\omega} [\hat{S}(\omega)]^{S(\omega)/\omega\hbar}, \quad (12)$$

or

$$LL = \ln L = \sum_{\omega} \frac{1}{\omega\hbar} S(\omega) \ln \hat{S}(\omega) \approx \frac{1}{\omega_{HF}\hbar} \sum_{\omega} S(\omega) \ln \hat{S}(\omega). \quad (13)$$

The last approximation accounts for $\omega = \omega_{\text{HF}} + \omega_{\text{D}} \approx \omega_{\text{HF}}$. Here ω_{HF} is the angular frequency of the HF system under observation, ω_{D} is the observed Doppler frequency and \ln is the natural logarithm.

Standard procedures of statistical physics for obtaining equilibrium distributions are equivalent in our case to maximizing the log-likelihood (LL) subject to a constraint on the overall number of photons, which is approximately equivalent in our case to energy constraint because $\omega \approx \omega_{\text{HF}}$:

$$\begin{cases} \max \text{ LL} \\ \sum_{\omega} S(\omega) = \sum_{\omega} \hat{S}(\omega) \end{cases} \quad (14)$$

It is interesting to note that the solution to this problem is mathematically equivalent to another, currently popular, deterministic problem of curve fitting using the Kullback-Leibler distance [6]. For this approach, according to the deterministic interpretation, MLANS chooses the spectral model parameters to minimize the Kullback-Leibler distance

$$\text{Min}_{\{A_m, \beta_m; 1 \leq m \leq M\}} \left\{ \sum_{n=1}^N S(\omega_n) \cdot \ln[S(\omega_n)/\hat{S}(\omega_n)] + \left[\int_{\omega} \hat{S}(\omega) d\omega - \sum_{n=1}^N S(\omega_n) \right] \right\}, \quad (15)$$

with the model spectrum given according to Equation (7) and β_m are the parameters of $F(\omega|m)$. This goodness-of-fit criterion is a measure of the closeness of the model spectrum to the measured spectrum, and it is also known as the cross-entropy. It can be shown that the minimum possible cross-entropy distance is zero, which occurs for the case where the model spectrum is exactly equal to the measured spectrum. It should be noted that the popular reference to Kullback-Leibler distance as a cross-entropy is based on historical analogies rather than on physical definition of entropy. According to the basic principles of statistical physics, the entropy of photons is maximized subject to physical constraints, leading to the maximum likelihood estimation.

Eliminating the redundant terms in Equation (15), and multiplying by minus-one converts the minimization problem into an equivalent maximization problem,

$$\text{Max}_{\{A_m, \beta_m; 1 \leq m \leq M\}} \left\{ \sum_{n=1}^N S(\omega_n) \cdot \ln \hat{S}(\omega_n) - \int_{\omega} \hat{S}(\omega) d\omega \right\}. \quad (16)$$

Substituting Equation (7) into Equation (6), and utilizing the following identity, recalling that the basis functions are normalized to have unit-area,

$$\int_{\omega} \hat{S}(\omega) d\omega = \sum_{m=1}^M A_m, \quad (17)$$

gives the complete maximization problem,

$$\text{Max}_{\{A_m, \beta_m; 1 \leq m \leq M\}} \left\{ \sum_{n=1}^N S(\omega_n) \cdot \ln \left[\sum_{m=1}^M A_m \cdot F_m(\omega_n | \beta_m) \right] - \sum_{m=1}^M A_m \right\}. \quad (18)$$

Here we have used the notation $F_m(\omega_n | \beta_m) = F(\omega_n | m)$.

A direct attempt to perform the indicated maximization in Equation (18) by setting partial derivatives equal to zero results in an intractable set of coupled nonlinear equations to solve. Instead, as previously discussed, MLANS utilizes an iterative procedure with the EM algorithm to perform the maximization. At the beginning of the k -th iteration, we have the model parameters from the previous iteration, $\{A_m^{(k-1)}, \beta_m^{(k-1)}; 1 \leq m \leq M\}$. The updated model parameters are found by performing the following maximization:

$$\text{Max}_{\{A_m^{(k)}, \beta_m^{(k)}; 1 \leq m \leq M\}} \left\{ \sum_{m=1}^M \left[\sum_{n=1}^N S(\omega_n) \cdot p(m | S(\omega_n); A_m^{(k-1)}, \beta_m^{(k-1)}) \cdot \ln [A_m^{(k)} \cdot F_m(\omega_n | \beta_m^{(k)})] - A_m^{(k)} \right] \right\}, \quad (19)$$

where

$$p(m | S(\omega_n); A_m^{(k-1)}, \beta_m^{(k-1)}) \equiv \frac{A_m^{(k-1)} \cdot F_m(\omega_n | \beta_m^{(k-1)})}{\sum_{j=1}^M A_j^{(k-1)} \cdot F_j(\omega_n | \beta_j^{(k-1)})}, \quad 1 \leq n \leq N, 1 \leq m \leq M. \quad (20)$$

It is convenient to refer to the above quantity shown by Equation (20) as a "fuzzy probabilistic association weight." It can be regarded as a measure of the degree of association of the m -th basis function with the n -th measurement. Note that for any fixed n , the sum of the fuzzy weights over m is equal to one.

The maximization task of Equation (19) is considerably easier than the maximization task in Equation (18) because the problem decouples over the different basis functions, i.e., the parameter updates can be found independently for each basis function. Setting the derivative of Equation (19) with respect to $A_m^{(k)}$ equal to zero gives the updated amplitude,

$$A_m^{(k)} = \sum_{n=1}^N S(\omega_n) \cdot p(m|S(\omega_n); A_m^{(k-1)}, \beta_m^{(k-1)}), \quad 1 \leq m \leq M. \quad (21)$$

The updated shape parameters are found by maximizing Equation (19) with respect to each of the $\beta_m^{(k)}$,

$$\text{Max}_{\beta_m^{(k)}} \left\{ \sum_{n=1}^N S(\omega_n) \cdot p(m|S(\omega_n); A_m^{(k-1)}, \beta_m^{(k-1)}) \cdot \ln[F_m(\omega_n | \beta_m^{(k)})] \right\}, \quad 1 \leq m \leq M. \quad (22)$$

For the Gaussian basis function given by Equation (9), the optimization can be carried out exactly; substituting Equation (9) into Equation (22), setting derivatives with respect to $\omega_m^{(k)}$ and $\Delta\omega_m^{(k)}$ equal to zero, and utilizing Equation (21) gives

$$\omega_m^{(k)} = \frac{\sum_{n=1}^N S(\omega_n) \cdot p(m|S(\omega_n); A_m^{(k-1)}, \beta_m^{(k-1)}) \cdot \omega_n}{A_m^{(k)}}, \quad 1 \leq m \leq M, \quad (23)$$

$$\Delta\omega_m^{(k)} = \left[\frac{\sum_{n=1}^N S(\omega_n) \cdot p(m|S(\omega_n); A_m^{(k-1)}, \beta_m^{(k-1)}) \cdot (\omega_n - \omega_m^{(k)})^2}{A_m^{(k)}} \right]^{1/2}, \quad 1 \leq m \leq M. \quad (24)$$

The expectation-maximization (EM) algorithm is summarized in pictorial form in Figure 1 as follows:

- (1) provide initial values for the parameters, $\{A_m^{(0)}, \beta_m^{(0)}; 1 \leq m \leq M\}$;
- (2) for $k \geq 1$, perform the k -th iteration as follows:
 - (a) begin with $\{A_m^{(k-1)}, \beta_m^{(k-1)}; 1 \leq m \leq M\}$;
 - (b) update the fuzzy probabilistic association weights according to Equation (20);
 - (c) update the basis function amplitudes according to Equation (21);
 - (d) update the basis function shape parameters by performing the maximizations in Equation (22) (For the uniform basis functions there are no shape parameters; for the Gaussian basis functions, the closed-form analytical formulas Equation (23) and Equation (24) are used.);
 - (e) end with $\{A_m^{(k)}, \beta_m^{(k)}; 1 \leq m \leq M\}$;
- (3) continue the iterations until convergence occurs.

The EM algorithm is not an intuitively obvious algorithm, and it is certainly not obvious that the iterative maximization in Equation (19) solves the maximization problem in Equation (18). However it can be proved in general that the sequence of parameter values provided by EM, $\{A_m^{(k)}, \beta_m^{(k)}; 1 \leq m \leq M\}$, converges to at least a local maximum of the goodness-of-fit criterion in Equation (18). See Appendix A for a detailed discussion and proof of convergence. In short, the EM algorithm is a "safe" iterative scheme.

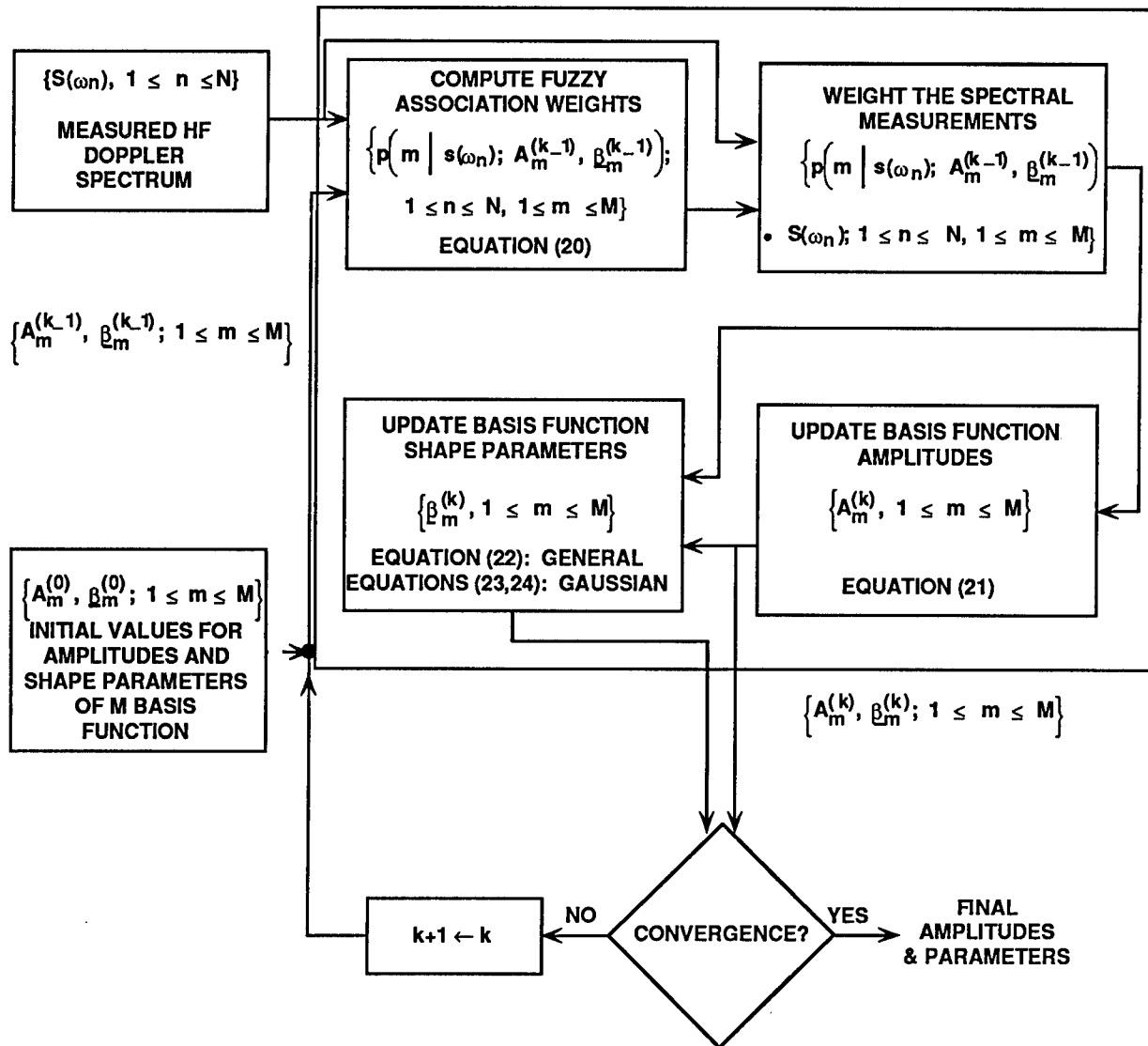


Figure 1. MLANS Application to Modeling HF Doppler Spectra

SECTION 3. RESULTS AND DISCUSSION

3.1 REPRESENTATIVE HF RADAR DATA

A sample HF radar return spectra set used in this study is shown in Figure 2. This figure shows a sequence of radar Doppler return spectra displayed as a function of Doppler cell number, spectrum number, and intensity on the color-coded, vertical axis. The image sequence in Figure 2 is from the ECRS OTH-B radar located in the state of Maine. It was recorded on 2 January 1992 as a part of the normal operational application of the ECRS, as were all radar data used in this study. The notation B34 refers to the radar beam directed to radar Segment 3, Sector 4, which corresponds to an azimuth of 162.75 degrees from the radar site in Maine [7,8]. The notation RB 1 refers to the first range bin (RB), which for this B34 data set has a start range of 1542 nautical miles (nm) from the radar site for the parameters for which the radar was being

operated. Under normal operation, the total range extent or foot print of the radar is nominally 500 nm. With the Doppler spectra averaged into 16 range bins, a single range bin for the OTH-B radar system is thus approximately 32 nm in extent. Each receive beam is 2.5 degrees wide in azimuth.

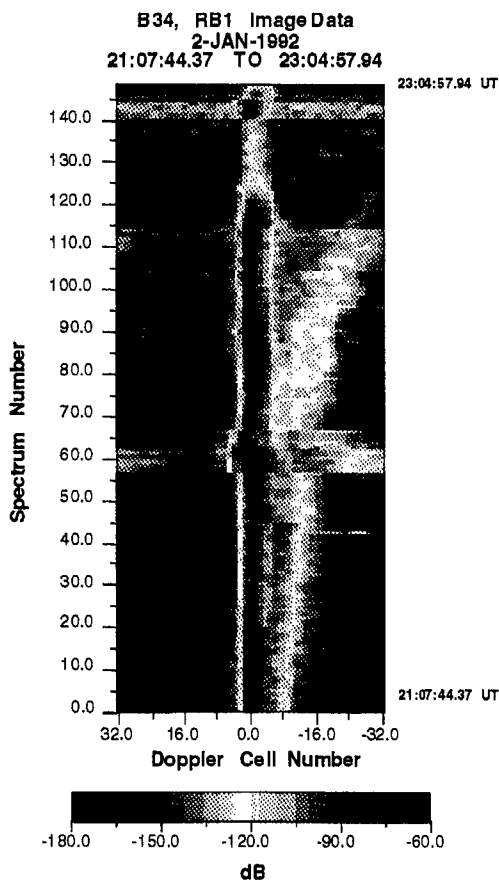


Figure 2. Sample HF Radar Doppler Spectra Data Set

The spectrum number is a sequential number which uniquely identifies a specific spectrum in the image sequence. There is a direct relationship, although nonlinear, between the spectrum number and the time a specific spectrum was recorded. For example, in Figure 2 the time changes from 21:07:44.37 UT for spectrum number 1 to 23:04:57.94 UT for spectrum number 149. The time associated with each spectrum is provided with individual spectra shown and discussed herein, along with the specific radar operating parameters.

The relationship between the Doppler cell number and the Doppler speed in meters per second (m/s) is given by

$$\text{Doppler speed} = c(\text{Doppler Cell Number}) / 2 f(\text{CIT}), \quad (25)$$

where c is the speed of light in m/s, f is the radar frequency in Hertz, and CIT is the coherent integration time in seconds. For radar targets such as aircraft, this is the observed radial speed, with negative values for outbound aircraft and positive values for inbound aircraft. For all the ECRS displays, negative Doppler is on the right, not the left. The Doppler speed for a clutter event is its apparent Doppler speed, which depends upon the spatial motion of the clutter event within the ionosphere. For convenience, all data analyses for this study were performed with the Doppler cell number scale. Each individual radar return spectrum can easily be converted to actual Doppler speed with the above equation, and this conversion is included in the radar image sequences and Doppler spectra contained herein.

The radar image sequence in Figure 2 is typical for the OTH-B radar when directed in a southerly direction. Observed in all OTH-B spectra, independent of the azimuth direction, is the extremely high intensity ground clutter return at near zero Doppler. Of particular interest for this study is the clutter event of lower intensity, starting in Figure 2 at low negative Doppler cell number and shifting to higher negative Doppler values as time progresses. This type of clutter structure is termed an "equatorial clutter event". The term "equatorial" implies that these types of clutter events are observed when the radar beam is directed in a southerly direction. For example, as mentioned above, the azimuth direction for this image sequence is 162.75 degrees. The physical cause of this type of clutter event is not being examined in the Phase 1 portion of this research effort. The ability to characterize and segment this clutter structure utilizing the MLANS neural network with a multi-modal Gaussian model for the clutter structure is the focus of this Phase 1 research effort.

We use the term "characterize" to denote the ability of employing a multi-mode Gaussian clutter model within MLANS to fit or describe the clutter structure contained in the Doppler spectra. The verb "segment" is used to denote the ability of the MLANS neural network to separate the equatorial structure from other clutter events, such as the ground clutter return and the background clutter. The ability of using the MLANS model-based neural network to accomplish clutter characterization and segmentation is important for operational applications

such as target detection and tracking in the presence of such clutter events (i.e., for low signal-to-clutter conditions). Also, it is important to be able to characterize and segment the clutter in order to study the specific properties of the clutter events.

Also observed in Figure 2 are radar "drop-out periods," for example, between spectrum numbers 57 to 66 and approximately 115 to 150. These are times when the OTH-B radar operators were adjusting the operational parameters, i.e., the waveform repetition frequency of the radar, in order to eliminate the multi-hop clutter and facilitate target detection and tracking. Large equatorial clutter events such as in Figure 2 can mask the smaller target returns, greatly reducing the radar's probability of detection and complicating the track initiation and track maintenance tasks. The long range objective of this research effort is to use the MLANS model-based neural network to identify and adaptively segment such clutter structures, thereby increasing the probability of detection and track of targets observed in the vicinity of these strong clutter events. The radar drop-out periods are of no direct interest to this Phase 1 portion of this research effort, except to be cognizant that the radar operating parameters are being changed during such time periods. Changed radar parameters may result in a change in the Doppler speed scale since the Doppler speed depends upon the Doppler cell number.

The specific Doppler spectrum in Figure 2 for spectrum number 25 is shown in Figure 3. This Doppler spectrum was recorded on 2 January 1992 at 21:23:49.88 UT, with the radar operating at 25.680 MHz, a CIT of 1.7778 seconds, and waveform repetition frequency (WRF) of 36.0 Hz. One sees the very large ground return peak at zero Doppler with the equatorial clutter structure centered at Doppler cell numbers approximately 6 to 12. The remainder of this spectrum is typical in that the background clutter is orders of magnitude below both the ground return and the equatorial structure. Background clutter is caused by such phenomena as meteors transiting the ionosphere, magnetic field-aligned ionospheric irregularities, and lightning events. No target returns are observed in this spectrum.

The following sections contain the results of the application of the MLANS model-based neural network to the OTH-B radar spectra similar to that shown in Figure 3 for clutter characterization and segmentation.

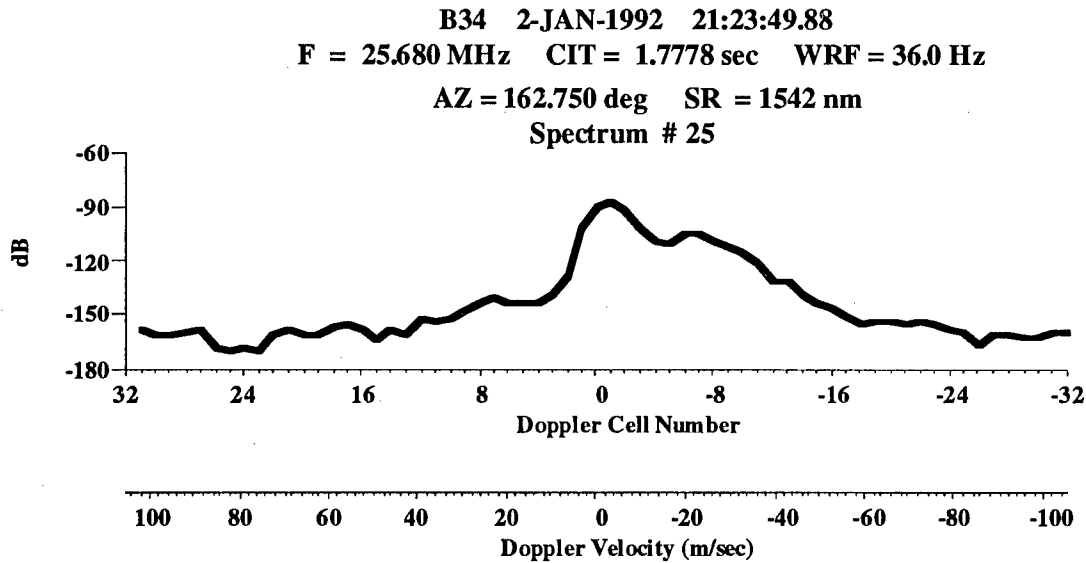


Figure 3. Representative Radar Doppler Spectrum

3.2. CLUTTER SEGMENTATION RESULTS

The MLANS neural network with the multi-modal Gaussian formulation plus uniform clutter model as described in Section 2 was applied to the individual radar Doppler spectra. Three- and four-mode Gaussian models were fitted to the data. A three-mode formulation was selected based on results of initial fits which showed that two modes were necessary to fit the ground return portion of the spectrum, leaving the third mode to describe the equatorial clutter structure. Four-mode fits were then obtained in order to provide an additional mode for further description of the clutter. The results of these analyses are shown and discussed below.

The analysis for this study was performed in the linear amplitude space rather than in a logarithmic space (dB). All spectra were first converted from dB to linear radar intensity, with the MLANS iterative fits being performed in this space, followed by conversion back to dB for plotting and display purposes. It is best to plot the Doppler spectra in dB due to the enormous differences in magnitude between the ground return peak and other observed events such as clutter structures and target returns.

3.2.1 3-Mode Gaussian Clutter Model

Representative results of the MLANS fits to the radar Doppler return spectra for various spectrum numbers for the B34, RB 1 data set in Figure 2 are shown in Figures 4 and 5. As sample spectra fits, we have shown representative fits for low spectrum numbers in Figure 4, while Figure 5 contains representative fits for a later time frame when this equatorial clutter event has further evolved. Range bin 1 has a start range of 1542 nm, and this data is for a radar beam direction of 162.75 degrees. This corresponds to ground surveillance of an area near Puerto Rico in the Caribbean. The red line in each plot is the sum of the three separate Gaussian modes plus a uniform background mode. As mentioned previously, this MLANS analysis and summation of the individual modes is performed in linear amplitude space, with the results being converted back to dB for plotting purposes.

The ground return clutter peak near zero Doppler cell number is seen to be well described by two Gaussian modes. This is conjectured to be due to the combination of the single-hop return (labeled as 'Primary Gaussian Center Mode') with an adjacent lower intensity, two-hop return (labeled as 'Secondary Gaussian Center Mode'), which can be a typical operational mode for OTH radar systems. This ground return structure could also be composed of additional hop returns of decreased intensity. An artist's sketch of the radar beam propagation illustrating multiple hops is contained in Figure 6.

With the ground return taking two of the three modes available, this leaves a single Gaussian mode (labeled as 'Remaining Gaussian Mode') to fit the equatorial clutter structure. This single-mode Gaussian fit to the equatorial clutter is seen to accurately describe the general nature of the clutter in terms of Doppler speed, magnitude and width. This single-mode model does not follow the fine structure of the clutter, nor would it be expected to do so. Also, it is not important that the clutter model describe this fine structure. These fine structure variations in the shape of the equatorial clutter are expected to be transient in nature, caused by the same phenomena that produces the background clutter as mentioned above. If target returns are associated with the equatorial clutter structure, then they will be persistent as a function of time, displaying the expected spatial variations of an aircraft target. Such persistent structure associated with the equatorial clutter can be detected and tracked utilizing the MLANS simultaneous detecting and tracking feature.

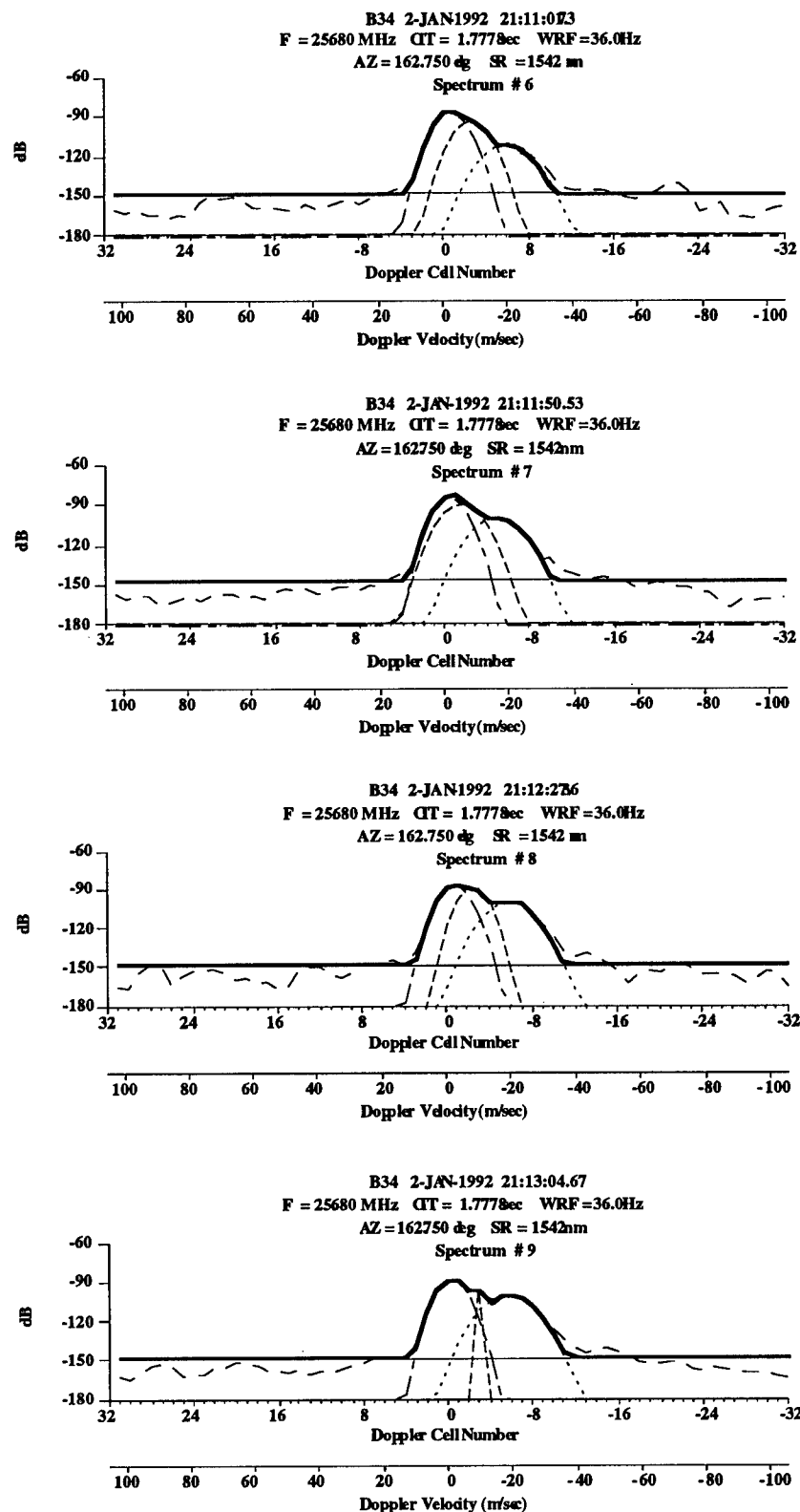
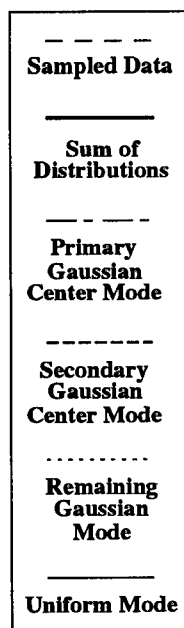


Figure 4. Three-Mode Gaussian Model Fits for Spectrum Numbers 6-9, B34, RB1 Data Set. A Single Uniform Model is Also Included.

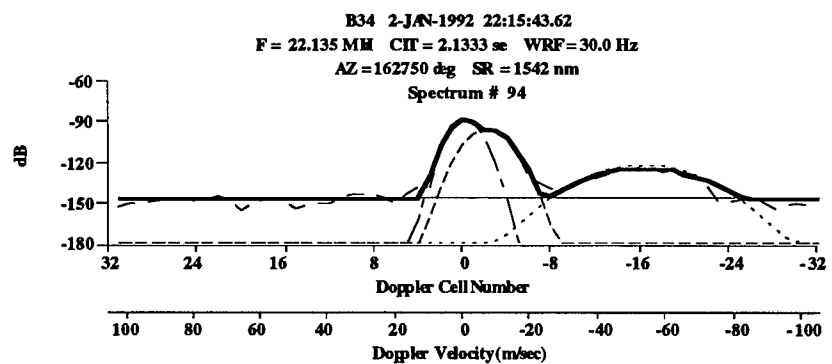
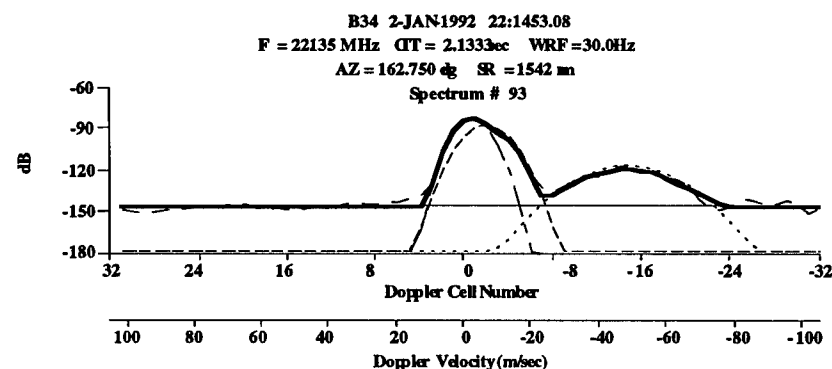
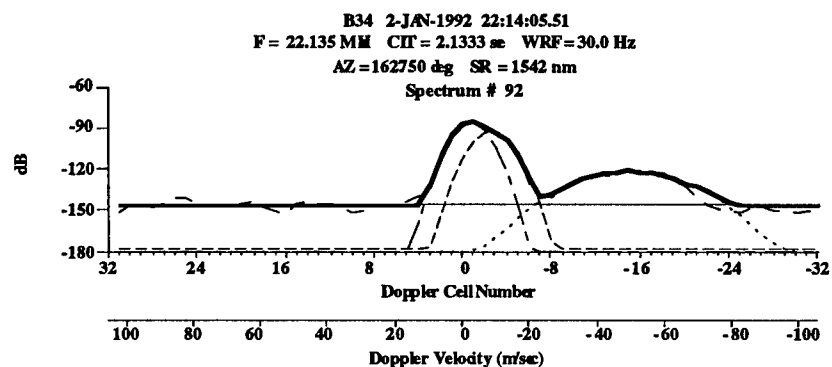
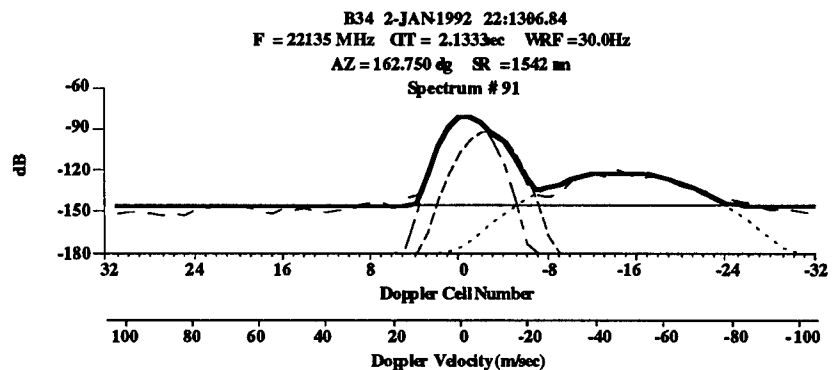
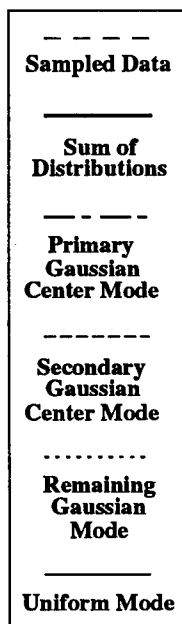


Figure 5. Three-Mode Gaussian Model Fits for Spectrum Numbers 91-94, B34, RB1 Data Set.
 A Single Uniform Model is Also Included.

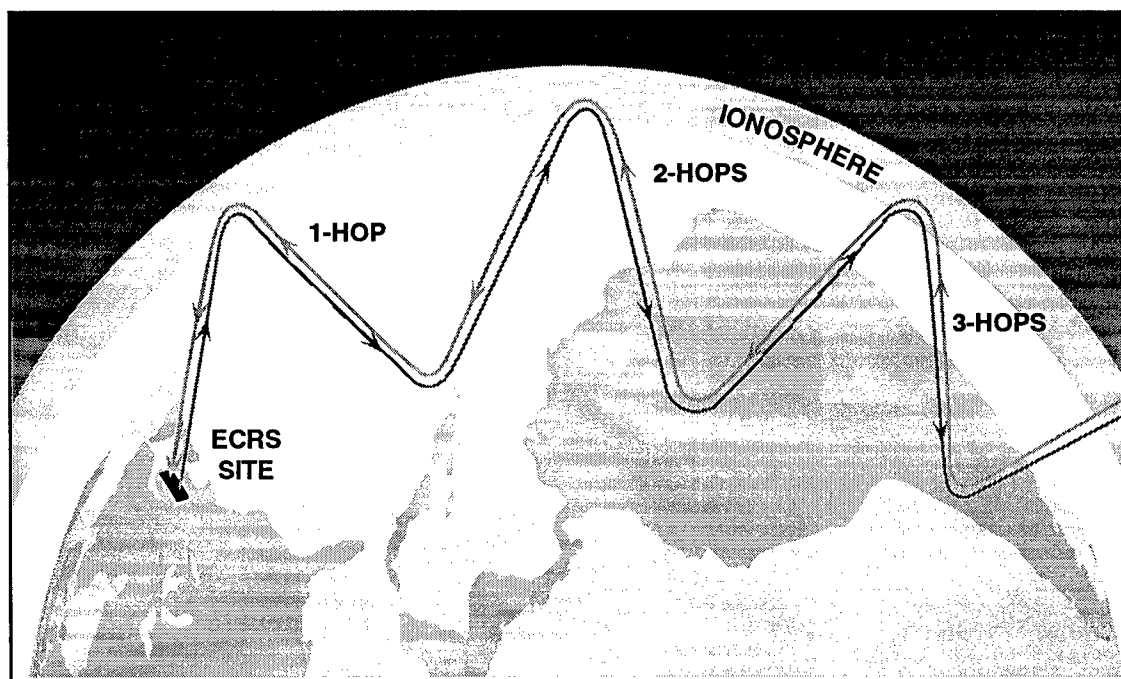


Figure 6. Artist's Sketch of the Radar Beam Propagation with Multiple Hops

The uniform model used to describe the background clutter is seen also to be adequate to fit the fine structure variations observed in the background. Similar to the discussion above, it is not important to the objectives of this research project that an exact fit to the background clutter be obtained. Any aircraft target returns will persist in time and display the spatial variations expected. Also, it is important to recognize that the background clutter is many orders of magnitude less than the other spectrum structures, and will also be less in magnitude compared to target returns.

Figure 7 shows a comparison of the raw image data set from Figure 2 with that obtained from fits to all Doppler spectra within the image with the 3-mode Gaussian plus uniform model. The comparison of the model fit to the raw image is remarkably close considering the simplistic form of the Gaussian clutter model. This 3-mode Gaussian model is seen to track the overall clutter structure as a function of time for both the ground clutter and the equatorial clutter structures.

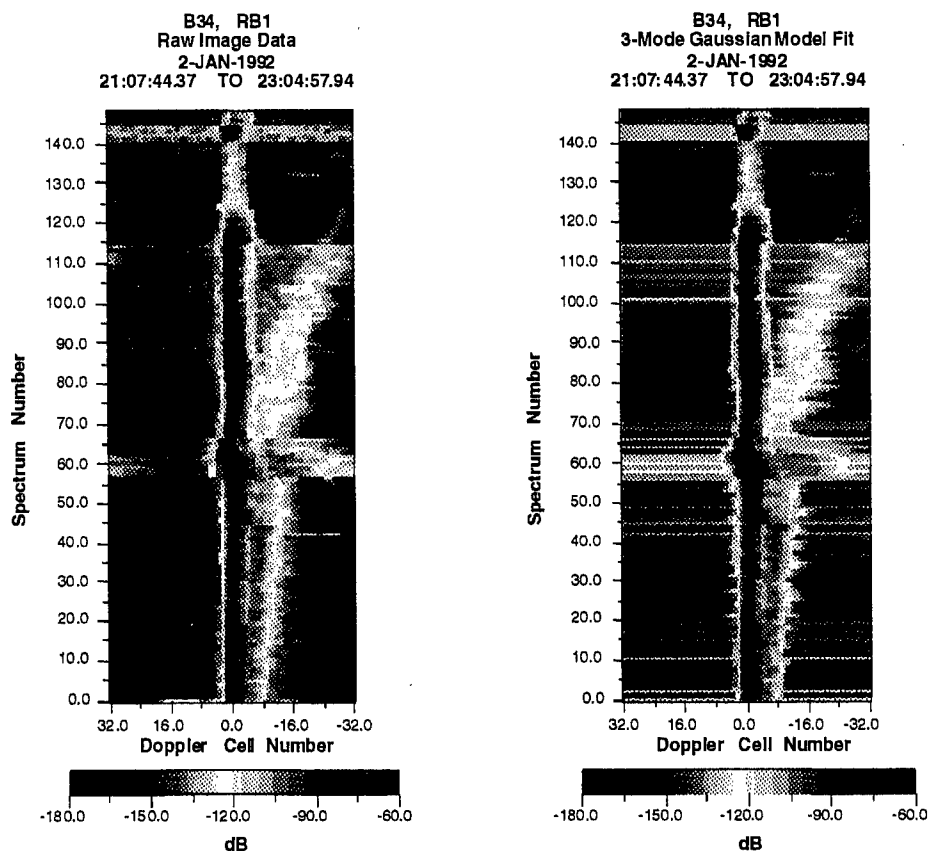


Figure 7. Consolidated Three-Mode Gaussian Model Fits and Raw Image Data for B34, RB1 Data Set

3.2.2 4-Mode Gaussian Clutter Model

Introduction of a 4-mode Gaussian clutter model provides for one additional Gaussian mode for describing the overall clutter structure. Results of the 4-mode fits, similar to those shown above for the 3-mode model, are contained in Figures 8 and 9. The fourth mode does in general provide for an additional Gaussian mode for describing the equatorial clutter structure. However, this is not always the case. For certain spectra, the fourth mode describes other structures in the spectra, which are usually transient. A good example is observed for the fit to spectrum number 6 shown in Figure 8. Here, the fourth mode (right-hand side 'Remaining Gaussian Mode') picked up the background transient event at Doppler cell number 21. However, in spectrum numbers 7, 8 and 9 this mode appears in Doppler cells 7, 7 and 10 respectively. This capability of MLANS to adapt to changing structures and events in the Doppler spectra will be important to operational application of MLANS for the detection and tracking function. But, for equatorial clutter structure characterization it is irrelevant.

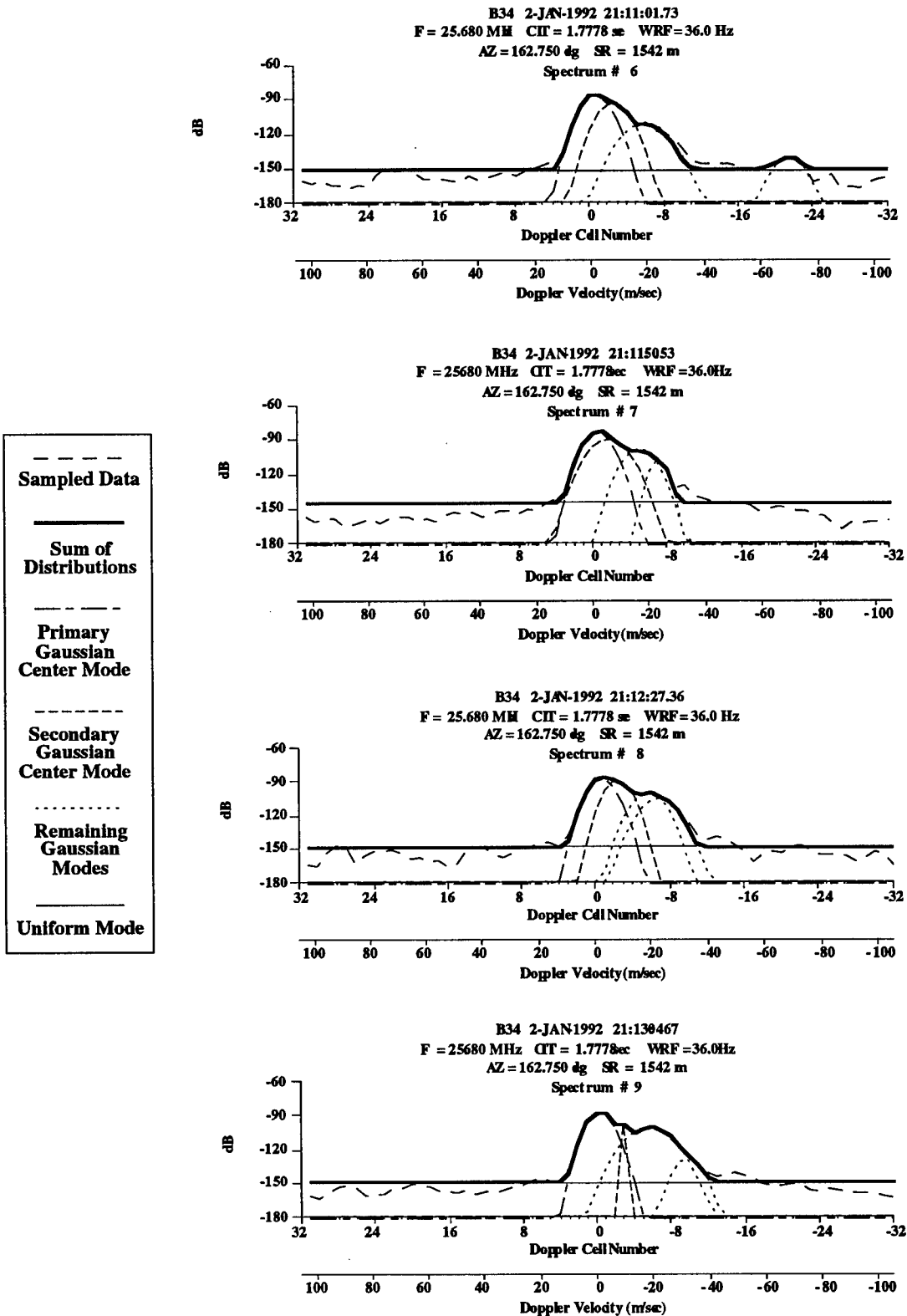


Figure 8. Four-Mode Gaussian Model Fits for Spectrum Numbers 6-9, B34, RB1 Data Set.

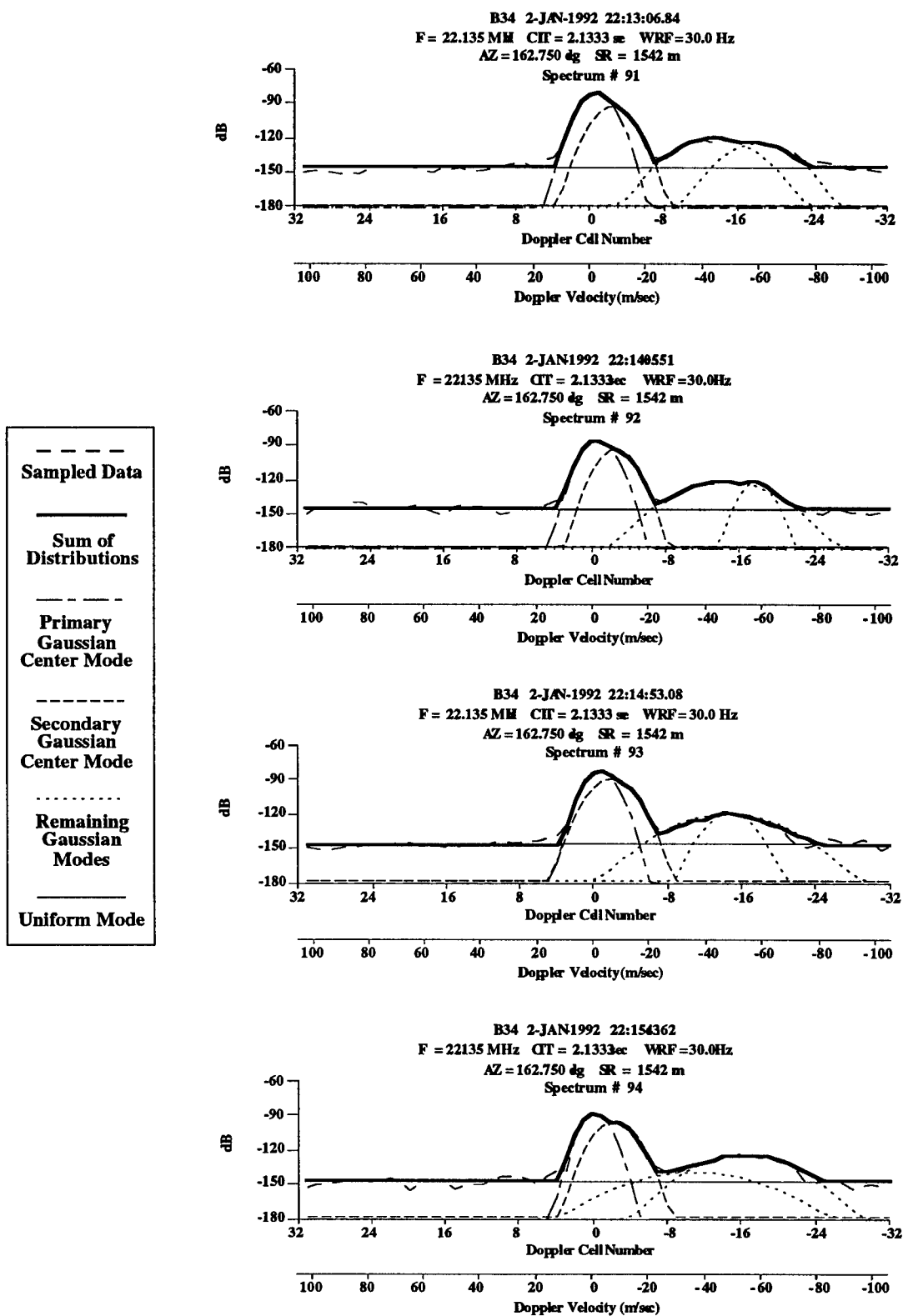


Figure 9. Four-Mode Gaussian Model Fits for Spectrum Numbers 91-94, B34, RB1 Data Set.

A consolidated comparison of the 4-mode model fit with the raw data image is shown in Figure 10. (Here the vertical axis is shown in gray scale, as are the remaining Doppler spectra data sets contained within this report.) As for the 3-mode case, the comparison is very good. However, the 4-mode model does not obviously provide a better fit than the 3-mode model. The results of these analyses thus do not indicate whether the four-mode model is better than the three-mode model. However, if persistent in time, small differences between the clutter and the data may be important for the detection and tracking function, which may make the higher mode model of MLANS more important for operational applications. A detailed study of the detection and tracking capability of MLANS is planned for the next phase of this research project.

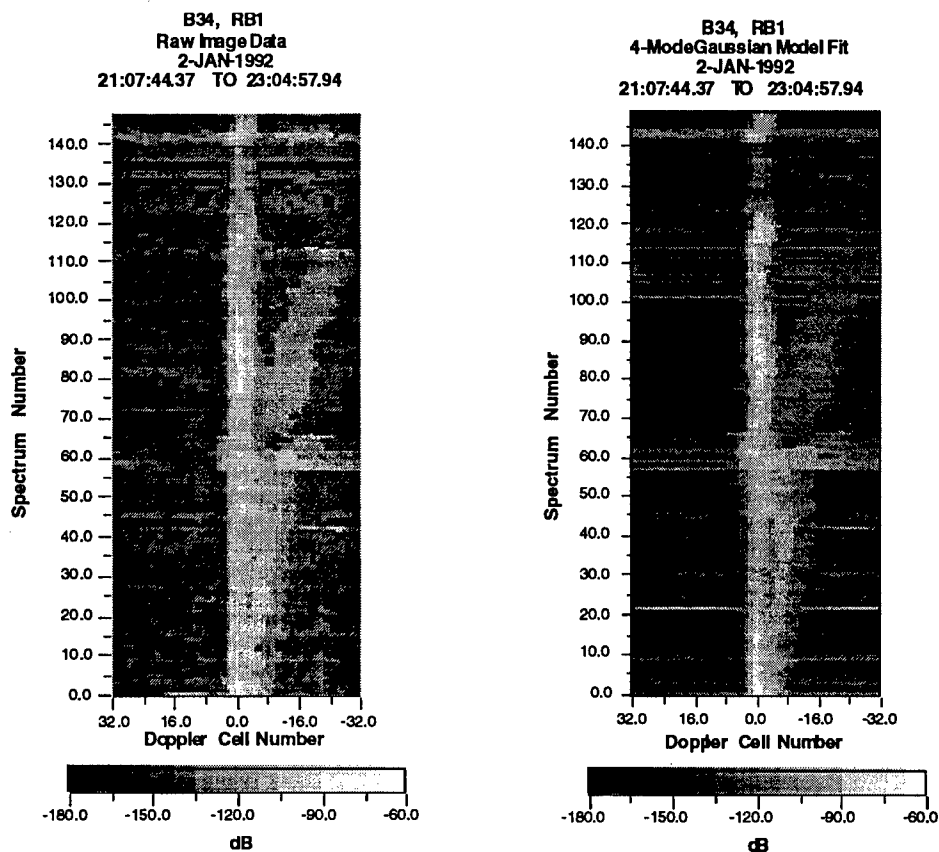


Figure 10. Consolidated Four-Mode Gaussian Model Fits and Raw Image Data for B34, RB1 Data Set

3.2.3. Model Parameter Functionality

The model parameters for the Gaussian model are the center Doppler frequency for each mode, the mode amplitude, and the mode variance or width. The center Doppler frequency and

mode width are expressed herein in units of Doppler cell number which can be simply converted to units of Hertz. The mode amplitude is expressed here in dB, but can simply be transformed to absolute magnitude.

The mode center frequencies for the 3-mode model are shown for the B34, RB 1 data set in Figure 11. As expected from the individual spectrum results shown and discussed above in Section 3.2.1, the mode center frequencies accurately describe and track the raw data as a function of time for the ground return clutter structure and for the observed equatorial clutter event. Two center frequencies near zero Doppler track the ground clutter return while a single mode tracks the equatorial clutter.

Similar results are obtained for the 4-mode model case as shown in Figure 12. Again, two modes track the ground return while the other two modes track the equatorial clutter.

Plots of the mode amplitudes as a function of spectrum number are shown in Figure 13 for both the 3-mode and 4-mode clutter models for the B34, RB 1 data set. This plot as a function of spectrum number is equivalent to plotting as a function of time since the spectrum number is directly related to time. The third mode of the 3-mode model, which describes the amplitude of the equatorial clutter event, is seen to be decreasing in time, from approximately -100 dB at the start of the event to about -120 dB at spectrum number 115 (the operating parameters of the radar were continuously being changed from spectrum number 115 to spectrum number 150), while the mode amplitude for the two modes tracking the ground return remain fairly constant at about -85 dB. The same conclusions are reached upon examining the mode amplitude variations for the 4-mode model fits.

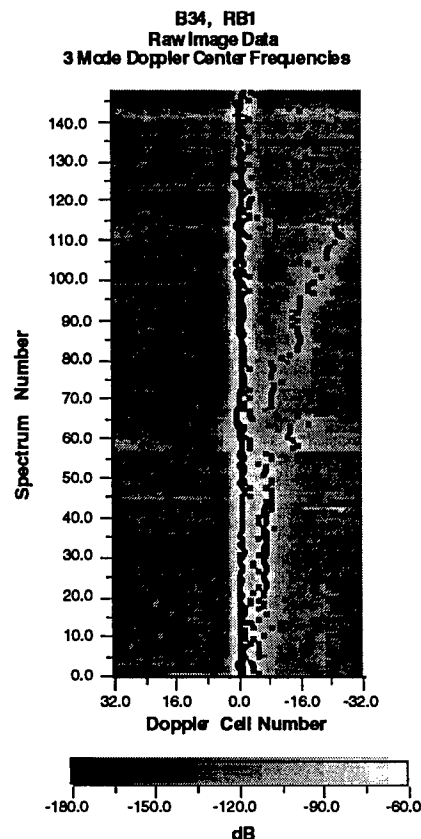


Figure 11. Plot of the Center Frequencies for the Three-Mode Gaussian Model as Compared to the Raw Image Data for B34, RB1 Data Set

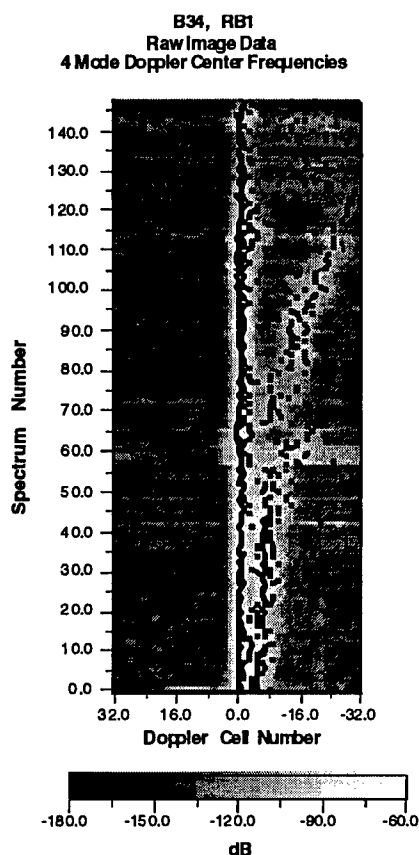


Figure 12. Plot of the Center Frequencies for the Four-Mode Gaussian Model as Compared to the Raw Image Data for B34, RB1 Data Set

An interesting aspect of the adaptability of the MLANS neural network is seen in Figure 13. The radar operational parameters were also being adjusted from about spectrum number 57 to 66, which resulted in the radar beam refracting at a different location within the ionosphere. A new operating regime for the radar was being sought during this time frame by the radar operators in order to reduce the magnitude of the equatorial clutter. The MLANS neural network was able to adaptively track this change in magnitude of the equatorial clutter structure while measuring a nearly constant amplitude for the ground clutter structure. In addition, it was able to adapt to the change in center frequency location over this time frame as observed in Figures 11 and 12 for spectrum numbers 57 to 66. This adaptive nature of MLANS will be important for detection and tracking applications.

Plots of the mode variance (width) as a function of spectrum number (as above, related to time) are shown in Figure 14 for both the 3-mode and 4-mode models for the B34, RB 1 data set. Both plots show that the variance for the two modes describing the ground return remain relatively small over the duration of the event while the variance for the mode (3-mode case) or modes (4-mode case) that describe the equatorial event start off small, but increase in magnitude as the clutter event evolves. This implies that the equatorial clutter structure is expanding spatially on a temporal basis.

B34, RB1 Gaussian Mode Amplitudes

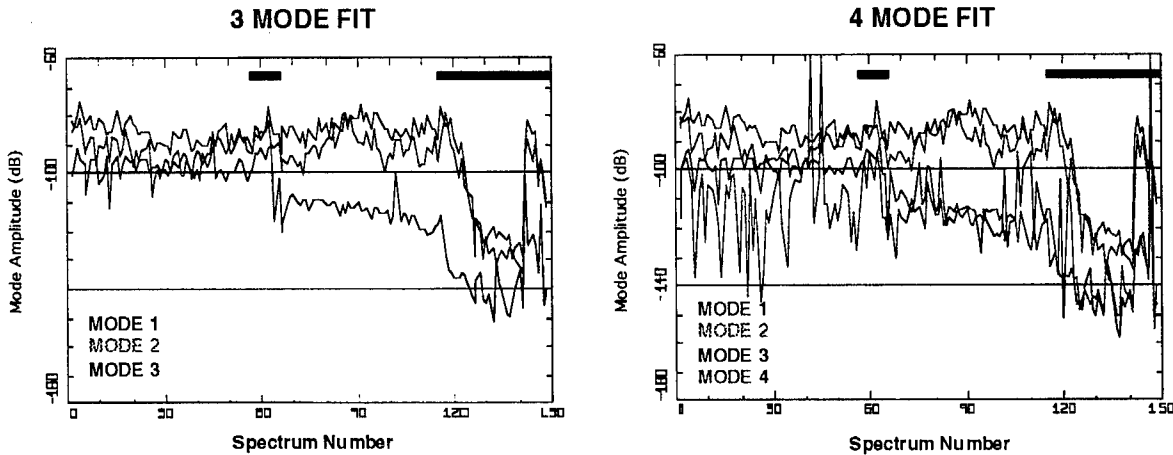


Figure 13. Plot of the Gaussian Mode Amplitudes for B34, RB1 Data Set

B34, RB1 Gaussian Mode Variances

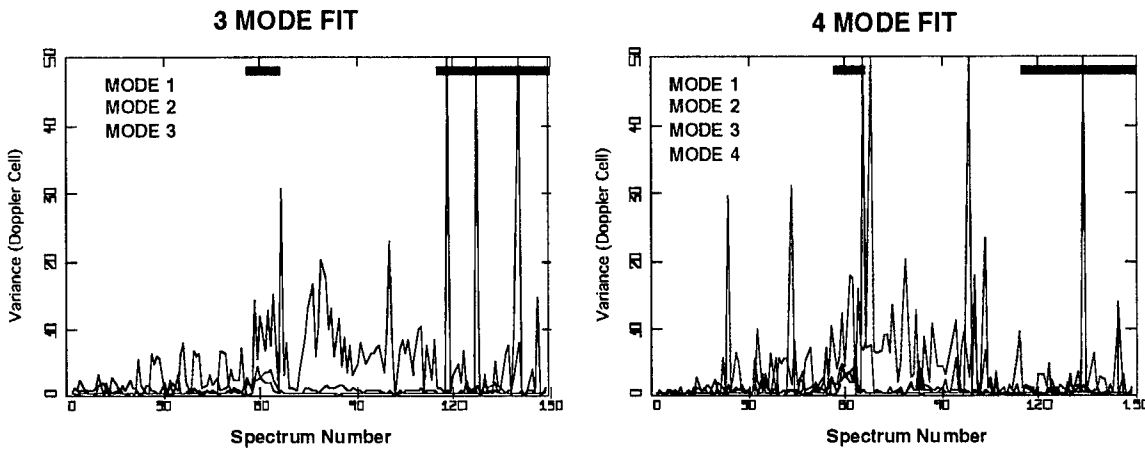


Figure 14. Plot of the Gaussian Mode Variances for B34, RB1 Data Set.
Black Bands at Top Indicate Periods of Operator Intervention.

Additional analyses at different ranges and azimuths were performed for the 3-mode clutter model for this same clutter event. For example, Figure 15 shows the comparison of the 3-mode model fit to the data for the B34, RB 9 data set. One sees again that the modeled image on the right side of Figure 15 very accurately describes the actual Doppler image data shown on the left side, until the clutter event was eliminated at spectrum number 115 by the radar operators by changing the operating parameters of the radar system. The mode center frequencies are also

plotted on the left side with the Doppler image. The mode functionalities for the mode amplitudes and variances for this image fit are similar to those described above for the B34, RB 1 data set.

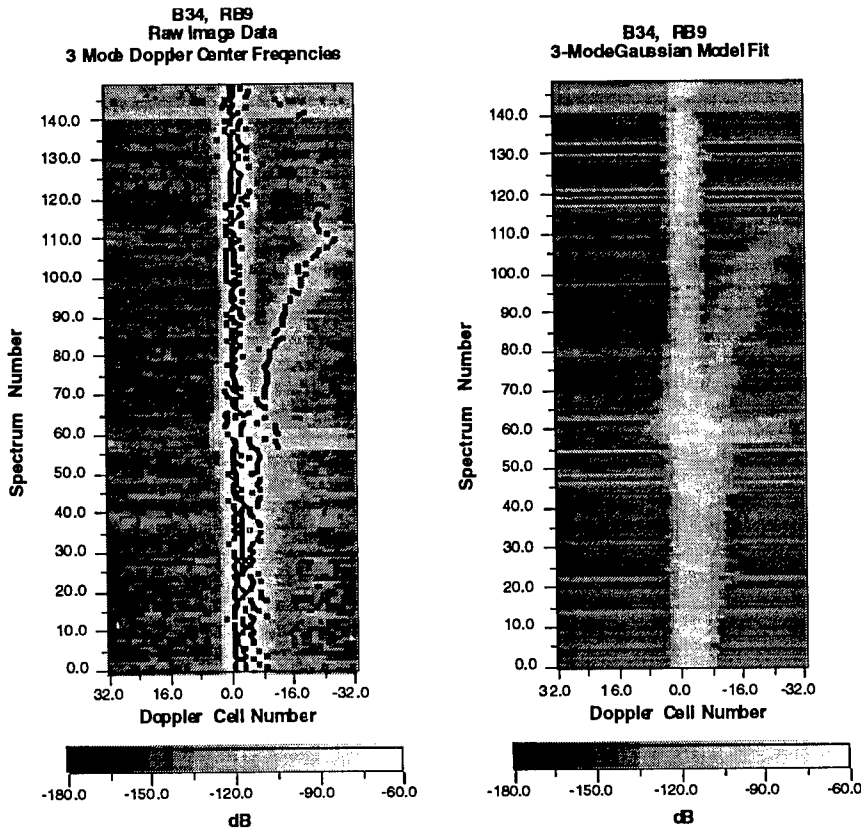


Figure 15. Consolidated Three-Mode Gaussian Model Fit and Raw Image Data for B34, RB9 Data Set. Also Shown Superimposed on the Raw Image Plot are the Center Frequencies for the Three-Mode Gaussian Model.

The results of a fit to a data set at a different azimuth are shown in Figure 16. These results are for the B36, RB 1 data set which corresponds to an azimuth of 177.75 degrees. The time evolution of the equatorial clutter is markedly different than for the B34, RB 1 data set previously discussed. As seen by the model fit on the right side and by the location of the mode center frequencies plotted with the image data on the left side of the figure, MLANS is able to describe the clutter structure as a function of time.

From these results, one sees that the MLANS neural network with a multi-modal Gaussian clutter model is able to characterize the clutter contained within the HF radar Doppler spectra. In addition, it is able to segment the equatorial and the ground return clutter structures.

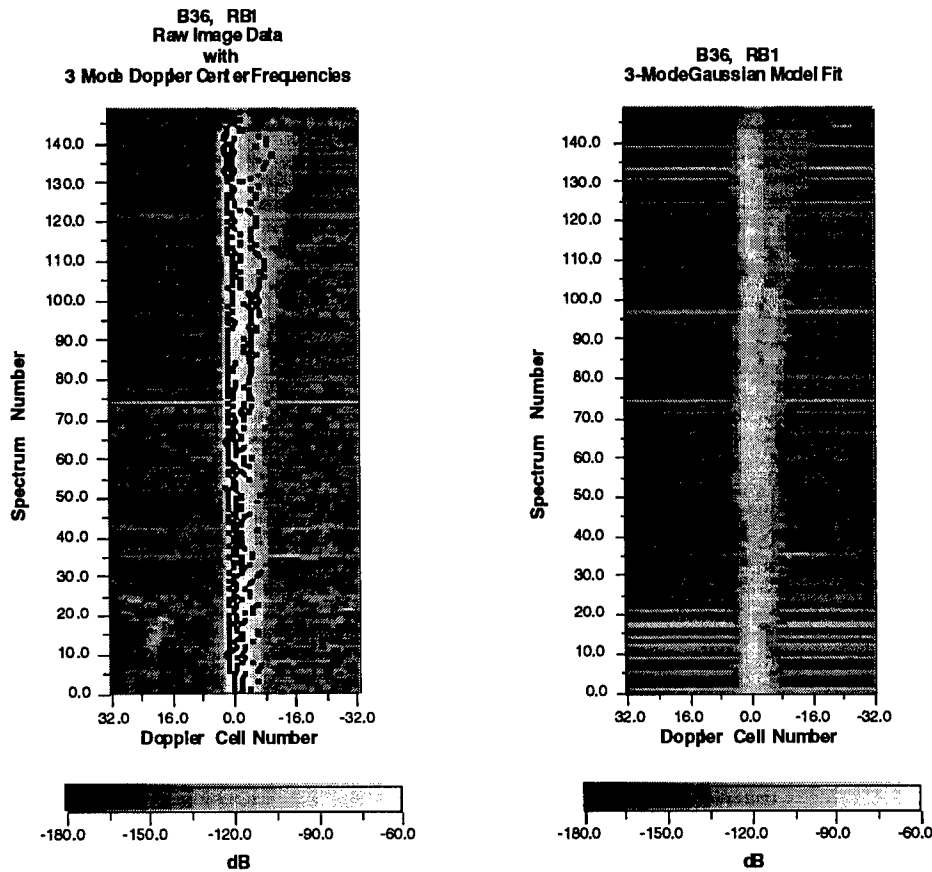


Figure 16. Consolidated Three-Mode Gaussian Model Fit and Raw Image Data for B36, RB1 Data Set. Also Shown Superimposed on the Raw Image Plot are the Center Frequencies for the Three-Mode Gaussian Model.

The 4-mode model, which uses two Gaussian modes to fit the equatorial clutter structure, was not determined to be superior to the 3-mode model which uses a single mode to fit the equatorial clutter. Determining the optimum number of modes to use to segment the clutter will have to await further investigations concerning the MLANS detection and tracking capability planned for the next phase of this research study.

3.2.4 Fits to Averaged Data

In order to investigate the effect that averaging the data has on the Gaussian model results, we averaged the spectra as a function of time and again fitted the averaged spectra with the MLANS multi-modal Gaussian model formulation. Although not expected to be useful for operational applications of MLANS to HF radar systems for enhanced detection and tracking,

averaging of the spectra should smooth out the short-term transient variations in the Doppler spectra, allowing for a better fit of the multi-mode Gaussian model to the clutter structures.

Sample averaged spectra results for averaging together of three spectrum numbers for the B34, RB 1 data set are shown in Figures 17 and 18. Figure 17 is the average of spectrum numbers 6, 7, and 8, while Figure 18 is the average of spectrum numbers 92, 93, and 94. As expected, these averaged spectra are smoother than the single spectra shown in Figures 4 and 5 above. The 3-mode Gaussian model fits along with the uniform model are also plotted in Figures 16 and 17, and are seen to well represent the data. As before, two Gaussian modes are used by MLANS to fit the ground clutter return while the remaining mode is used to describe the equatorial clutter structure. As expected for the averaged data, the uniform model does track the background more closely than for the unaveraged data.

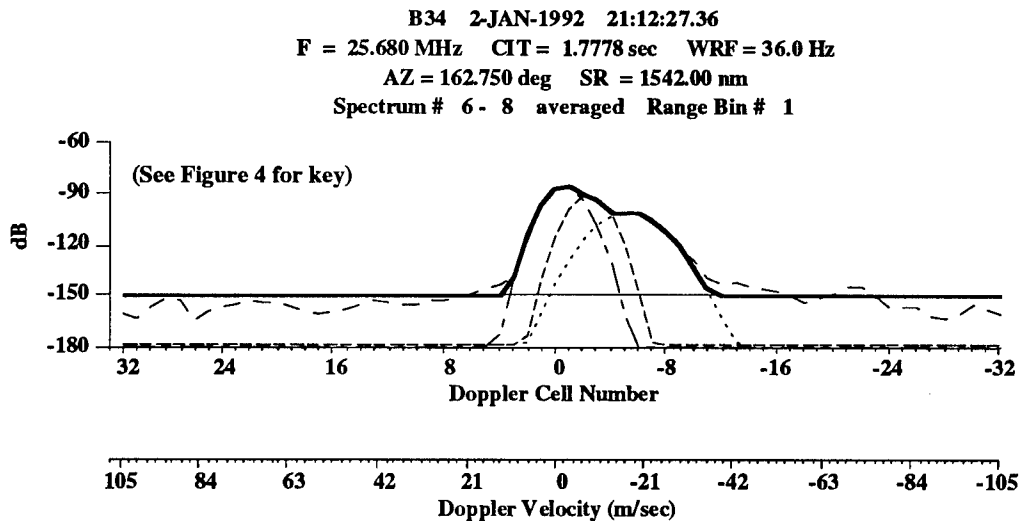


Figure 17. Three-Mode Gaussian Model Fits for Average of Spectrum Numbers 6, 7 and 8, B34, RB1

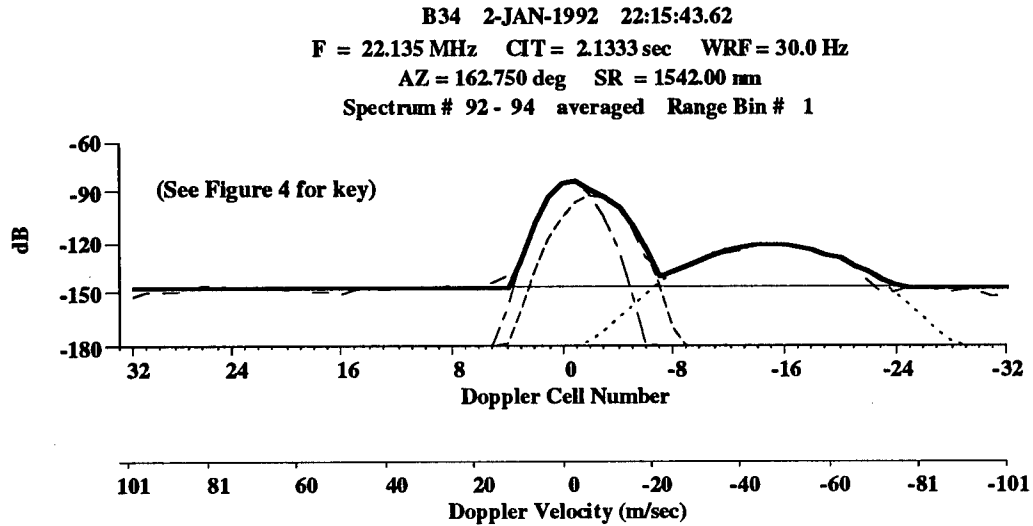


Figure 18. Three-Mode Gaussian Model Fits for Average of Spectrum Numbers 92, 93 and 94, B34, RB1

The consolidated image data for these averaged spectra are shown in Figure 19. The right side of this figure shows the 3-mode Gaussian model fit to the image, while the raw, averaged data is on the left side. The 3-mode model is seen to very accurately represent the raw data. Also plotted on the left side are the center frequencies for the three separate Gaussian modes. As for the unaveraged data shown in Figure 11, the 3-mode model tracks the time evolution of the data.

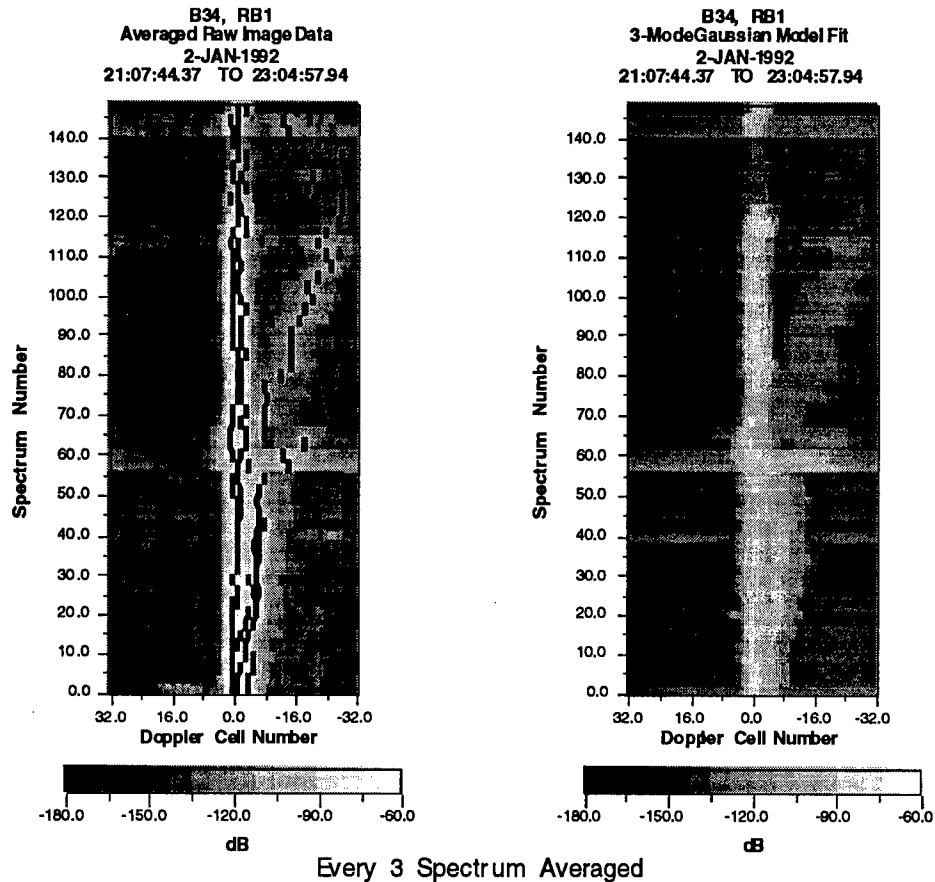


Figure 19. Consolidated Three-Mode Gaussian Model Fit and Raw Image Data for Three Spectrum Average of the B34, RB1 Data Set. Also Plotted on the Left Side are the Center Frequencies for the Three-Mode Gaussian Model.

The time dependence of the amplitude and variance parameters of the Gaussian modes are shown in Figures 20 and 21 for this fit to the averaged data. On examining these two figures, one reaches the same conclusions as in Section 3.2.3 concerning the time evolution of the equatorial clutter event being described by the third Gaussian mode; namely, that the equatorial clutter event decreases in magnitude and spreads out in Doppler frequency space as time evolves.

Upon examining the Gaussian model fit results for the averaged data as compared to the unaveraged data, one concludes that there is no further advantage to fitting averaging data except that smoother spectra are obtained with short-term variations washed out. The same conclusions were reached, with regard to the ability of the multi-modal Gaussian model to represent the data as presented above in Sections 3.2.1 through 3.2.3, as were concluded for the averaged data.

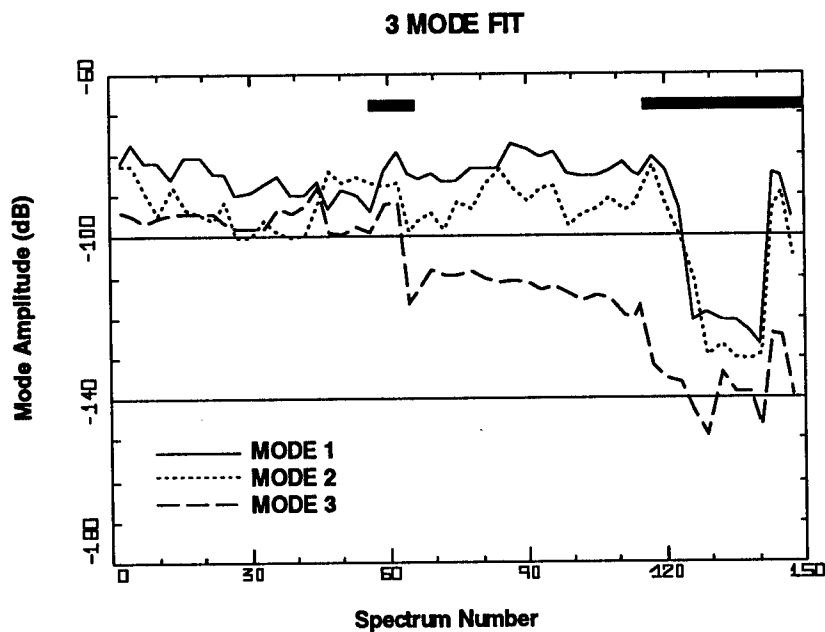


Figure 20. Plot of the Gaussian Mode Amplitudes for the Three Spectrum Average of the B34, RB1 Data Set

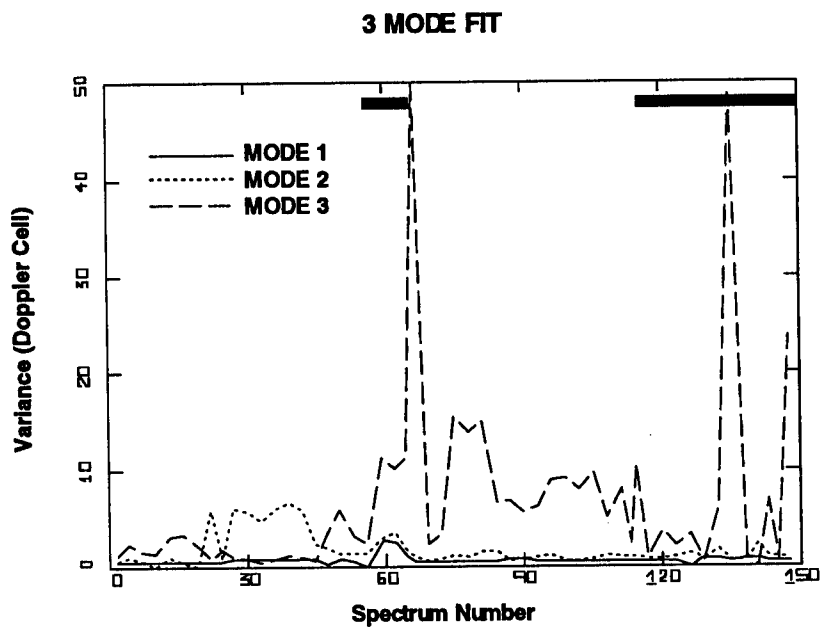


Figure 21. Plot of the Gaussian Mode Variances for the Three Spectrum Average of the B34, RB1 Data Set. Black Bands at Top Indicate Periods of Operator Intervention.

SECTION 4. CONCLUSIONS

The primary objective of this initial phase was to demonstrate the ability of the MLANS model-based neural network to segment and characterize clutter structures observed during the operation of an HF radar system. This objective was accomplished.

The study results enables one to draw several conclusions:

- (1) The MLANS model-based neural network is able to characterize the observed clutter structures with a multi-modal Gaussian clutter model. In fact, the equatorial clutter can be generally characterized by a single-mode Gaussian model obtained by applying a 3-mode Gaussian clutter model to the data, with two of the modes being used to describe the ground clutter return and the third mode being used to describe the equatorial clutter return.
- (2) The MLANS neural network is able to segment the ionospheric clutter structure, consistently separating the equatorial clutter structure from the ground clutter return.
- (3) Including additional Gaussian modes to describe the equatorial clutter does not significantly improve the characterization and segmentation process as was shown by the application of a 4-mode clutter model which provided an additional mode to further describe the observed clutter structures.
- (4) Results demonstrated herein show the capability to obtain trends in parameters for the multi-modal Gaussian clutter model as functions of time, Doppler frequency, range, and azimuth. From a more detailed analysis of such trends in the clutter model parameters, one could, for example, study specific aspects of ionospheric clutter such as its time and spatial evolution.

SECTION 5. RECOMMENDATIONS

The results and conclusions of this study lead to several recommendations. This study has shown that the MLANS neural network can be a very powerful analysis tool to investigate ionospheric clutter observed in the operation of HF radar systems. Also, with its capability to characterize and segment the observed clutter, MLANS demonstrates promise as a signal processing algorithm to enhance the detection and tracking capability of such radar systems. The study results were obtained using a simple multi-modal Gaussian model for the clutter structure.

The first recommendation is that the study be continued to provide a more detailed analysis of properties of equatorial clutter using HF radar data. We recommend that this be accomplished with the multi-modal Gaussian model, analyzing in detail all aspects of the equatorial clutter as described by the model. We also recommend this be accomplished in parallel with a similar analysis of the clutter by application of a more descriptive clutter model such as that provided by a power law formulation. This detailed study of the equatorial clutter structure would have the objective of determining the spatial and temporal dependencies of the parameters of the clutter models for specific clutter events.

We recommend that further study be conducted in application of the MLANS neural network as a simultaneous detection and tracking signal processing algorithm as described in Appendix B. This study should have as an objective an analysis of MLANS to detect and track targets in the vicinity of strong equatorial clutter events. Other aspects that could be investigated are automatic track initiation and detection and tracking of multiple targets.

REFERENCES

1. Carpenter, G.A. (1989). *Neural Network Models for Pattern Recognition and Associative Memory*. Neural Networks, 2, 243-257.
2. Perlovsky, L.I. & McManus, M.M. (1991). *Maximum Likelihood Neural Networks for Sensor Fusion and Adaptive Classification*. Neural Networks, 4(1), pp. 89-102.
3. Perlovsky, L.I. (1987). *Antisimulation for Penetration Aids*. Final Report for Period 16 July 1986 - 15 January 1987, Phase I SBIR, for HQ, Ballistic Missile Office.
4. Dempster, A. P., Laird, N. M. & Rubin, D. B. (1977). *Maximum Likelihood from Incomplete Data via the EM Algorithm*. Jour. Royal Statist. Society, Ser. B, Vol.39.
- * 5. Franchi, P.R. & Tichovolsky, E.J. (1989). *Phase Screen Modulation as a Source of Clutter Related Noise in Over-the-Horizon Radars*. RADC-TR-89-296, November 1989.
6. Byrne, C. L. (1993). *Iterative Image Reconstruction Algorithms Based on Cross-Entropy Minimization*. IEEE Trans. on Image Processing, Jan. 1993.
7. Sales, G. S. (1992). *OTH-B Radar System: System Summary*. PL-TR-92-2134, May 1992.
8. Sales, G. S. (1992). *High Frequency (HF) Radiowave Propagation*. PL-TR-92-2123, April 1992.
9. Blackman, S. S. (1986). *Multiple Target Tracking with Radar Applications*. Artech House, Norwood, MA.
10. Singer, R. A., Sea, R. G., and Housewright, R. B. (1974). *Derivation and Evaluation of Improved Tracking Filters for Use in Dense Multitarget Environments*. IEEE Transactions on Information Theory, IT-20, pp. 423-432.

*RADC-TR-89-296 is distribution limited to DOD and DOD contractors only; critical technology.

REFERENCES (Concluded)

11. Parra-Loera, R., Thompson, W.E., & Akbar, S.A. (1992). *Multilevel Distributed Fusion of Multisensor Data*. Conference on Signal Processing, Sensor Fusion and Target Recognition, SPIE Proceedings, Vol. 1699.
12. Bar-Shalom, Y. and Tse, E. (1975). *Tracking in a Cluttered Environment with Probabilistic Data Association*. Automatica, Vol. 11, pp. 451-460.
13. Marzetta, T. L. (1994). *Fan Filters, the 3-D Radon Transform and Image Sequence Analysis*. IEEE Trans. Image Processing, Vol. 3, no. 3, pp. 253-264, May 1994.

APPENDIX A. CONVERGENCE OF MLANS EM

The expectation-maximization (EM) iterative algorithm employed by MLANS for its parametric modeling of the HF Doppler spectrum converges to at least a local maximum of the goodness-of-fit criterion. Since it is difficult to find a simple, comprehensive discussion of the convergence properties in the literature we include such a discussion in this appendix.

Again the overall objective is to choose the basis function amplitudes and shape parameters to maximize the goodness-of-fit criterion in Equation (18),

$$\text{Max}_{\{A_m, \beta_m; 1 \leq m \leq M\}} \left\{ G(S|A, \beta) \right\}, \quad (\text{A1})$$

$$G(S|A, \beta) \equiv \left\{ \sum_{n=1}^N S(\omega_n) \cdot \ln \left[\sum_{m=1}^M A_m \cdot F_m(\omega_n | \beta_m) \right] - \sum_{m=1}^M A_m \right\}. \quad (\text{A2})$$

The EM algorithm begins its k -th iteration with the basis function amplitudes and shape parameters from the previous iteration, $\{A^{(k-1)}, \beta^{(k-1)}\}$, and it consists of two conceptually distinct steps: the E (expectation) step, and the M (maximization) step. The E-step consists of evaluating the expression

$$E(A, \beta; A^{(k-1)}, \beta^{(k-1)}) \equiv \left\{ \sum_{m=1}^M \left[\sum_{n=1}^N S(\omega_n) \cdot p(m|S(\omega_n); A_m^{(k-1)}, \beta_m^{(k-1)}) \cdot \ln [A_m \cdot F_m(\omega_n | \beta_m)] - A_m \right] \right\}, \quad (\text{A3})$$

where the fuzzy association weights are given by Equation (20). The M-step consists of maximizing the E-expression to obtain the updated amplitudes and shape parameters,

$$\text{Max}_{\{A_m^{(k)}, \beta_m^{(k)}; 1 \leq m \leq M\}} \left\{ E(A^{(k)}, \beta^{(k)}; A^{(k-1)}, \beta^{(k-1)}) \right\}. \quad (\text{A4})$$

We now state and prove two key properties of the EM algorithm. The first property states that the maximization step in Equation (A4) always results in an improved goodness-of-fit; in fact the property is somewhat stronger:

Property 1:

Within the k-th iteration of EM, for all amplitudes and shape parameters, $\{A, \beta\}$, such that

$$E(A, \beta; A^{(k-1)}, \beta^{(k-1)}) \underset{(\geq)}{>} E(A^{(k-1)}, \beta^{(k-1)}; A^{(k-1)}, \beta^{(k-1)}) . \quad (A5)$$

Note that $\{A, \beta\}$ do not have to be the global or even a local maximum for the E-expression. The corresponding goodness-of-fit is improved over the goodness-of-fit for the amplitudes and shape parameters of the previous iteration, such that

$$G(S|A, \beta) \underset{(\geq)}{>} G(S|A^{(k-1)}, \beta^{(k-1)}) . \quad (A6)$$

Proof:

Substituting the E-expression in Equation (A3) into both sides of Equation (A5), and subtracting the right-hand side from the left-hand side gives

$$\sum_{m=1}^M \left(\sum_{n=1}^N S(\omega_n) \cdot p(m|S(\omega_n); A_m^{(k-1)}, \beta_m^{(k-1)}) \cdot \ln \left[\frac{A_m \cdot F_m(\omega_n | \beta_m)}{A_m^{(k-1)} \cdot F_m(\omega_n | \beta_m^{(k-1)})} \right] - [A_m - A_m^{(k-1)}] \right) \underset{(\geq)}{>} 0. \quad (A7)$$

Since the logarithm is a convex function, any cord must lie below the curve itself. Equivalently if $\{\lambda_1, \dots, \lambda_M\}$ are a set of nonnegative weights that sum to one, then

$$\sum_{m=1}^M \lambda_m \ln(y_m) \leq \ln \left(\sum_{m=1}^M \lambda_m y_m \right), \quad (A8)$$

This property is also known as Jensen's inequality. Recalling that the fuzzy association weights are non-negative and that their summation over m is equal to one, we apply the inequality in Equation (A8) to the m-summation within Equation (A7) as follows,

$$\begin{aligned}
& \sum_{m=1}^M p(m|S(\omega_n); A_m^{(k-1)}, \beta_m^{(k-1)}) \cdot \ln \left[\frac{A_m \cdot F_m(\omega_n | \beta_m)}{A_m^{(k-1)} \cdot F_m(\omega_n | \beta_m^{(k-1)})} \right] \\
& \leq \ln \left[\sum_{m=1}^M p(m|S(\omega_n); A_m^{(k-1)}, \beta_m^{(k-1)}) \cdot \frac{A_m \cdot F_m(\omega_n | \beta_m)}{A_m^{(k-1)} \cdot F_m(\omega_n | \beta_m^{(k-1)})} \right]
\end{aligned} \tag{A9}$$

Substituting the expression for the fuzzy association weight in Equation (20) into the right-hand side of Equation (A9) and simplifying (Within the brackets, the numerator of the fuzzy weight cancels the denominator of the fraction.) gives

$$\begin{aligned}
& \sum_{m=1}^M p(m|S(\omega_n); A_m^{(k-1)}, \beta_m^{(k-1)}) \cdot \ln \left[\frac{A_m \cdot F_m(\omega_n | \beta_m)}{A_m^{(k-1)} \cdot F_m(\omega_n | \beta_m^{(k-1)})} \right] \\
& \leq \ln \left[\sum_{m=1}^M A_m \cdot F_m(\omega_n | \beta_m) \right] - \ln \left[\sum_{j=1}^M A_j^{(k-1)} \cdot F_j(\omega_n | \beta_j^{(k-1)}) \right].
\end{aligned} \tag{A10}$$

Replacing the m-summation within Equation (A7) with a larger quantity, e.g., the right-hand side of Equation (A10), results in an expression that still satisfies the inequality, i.e.

$$\begin{aligned}
& \sum_{n=1}^N S(\omega_n) \cdot \left(\ln \left[\sum_{m=1}^M A_m \cdot F_m(\omega_n | \beta_m) \right] - \ln \left[\sum_{j=1}^M A_j^{(k-1)} \cdot F_j(\omega_n | \beta_j^{(k-1)}) \right] \right) - \sum_{m=1}^M [A_m - A_m^{(k-1)}] \\
& \quad \geq 0,
\end{aligned} \tag{A11}$$

which is equivalent to Equation (A6).

Property 1 guarantees that the goodness-of-fit increases monotonically with each iteration; since it is upper-bounded, the goodness-of-fit must converge. Property 2 implies that the basis function amplitudes and shape parameters converge to a local maximum.

Property 2:

If, within the k -th iteration, $\{A=A^{(k-1)}, \underline{\beta}=\underline{\beta}^{(k-1)}\}$ is a local maximum of $E(A, \underline{\beta}; A^{(k-1)}, \underline{\beta}^{(k-1)})$, then $\{A=A^{(k-1)}, \underline{\beta}=\underline{\beta}^{(k-1)}\}$ is also a local maximum of $G(S|A, \underline{\beta})$.

Proof:

Combining the definitions in Equations (A2) and (A3) gives

$$\begin{aligned} E(A, \underline{\beta}; A^{(k-1)}, \underline{\beta}^{(k-1)}) &= G(S|A, \underline{\beta}) \\ &+ \sum_{n=1}^N S(\omega_n) \left\{ \sum_{m=1}^M p(m|S(\omega_n); A_m^{(k-1)}, \underline{\beta}_m^{(k-1)}) \cdot \ln [A_m \cdot F_m(\omega_n | \underline{\beta}_m)] - \ln \left[\sum_{j=1}^M A_j \cdot F_j(\omega_n | \underline{\beta}_j) \right] \right\} \\ &= G(S|A, \underline{\beta}) + \sum_{n=1}^N S(\omega_n) \left\{ \sum_{m=1}^M p(m|S(\omega_n); A_m^{(k-1)}, \underline{\beta}_m^{(k-1)}) \cdot \ln \left[\frac{A_m \cdot F_m(\omega_n | \underline{\beta}_m)}{\sum_{j=1}^M A_j \cdot F_j(\omega_n | \underline{\beta}_j)} \right] \right\}. \end{aligned} \quad (A12)$$

Considering the definition for the fuzzy association weight in Equation (20), the square-bracket expression in the right-hand side of Equation (A12) can be identified as

$$\left[\frac{A_m \cdot F_m(\omega_n | \underline{\beta}_m)}{\sum_{j=1}^M A_j \cdot F_j(\omega_n | \underline{\beta}_j)} \right] = p(m|S(\omega_n); A_m, \underline{\beta}_m). \quad (A13)$$

By assumption the partial derivatives of the left-hand side of Equation (A12) with respect to A and $\underline{\beta}$ are equal to zero for $\{A=A^{(k-1)}, \underline{\beta}=\underline{\beta}^{(k-1)}\}$; we need to show that the partial derivatives of the second term in the right-hand side of Equation (A12) vanish. The argument is as follows: let $p(m|a)$ be a nonnegative-valued sequence whose sum is equal to one; then

$$\begin{aligned} \frac{d}{da} \left\{ \sum_{m=1}^M p(m|a^{(k-1)}) \cdot \ln p(m|a) \right\}_{a=a^{(k-1)}} &= \left\{ \sum_{m=1}^M \frac{p(m|a^{(k-1)})}{p(m|a)} \frac{d}{da} p(m|a) \right\}_{a=a^{(k-1)}} \\ &= \sum_{m=1}^M \frac{d}{da^{(k-1)}} p(m|a^{(k-1)}) = \frac{d}{da^{(k-1)}} \sum_{m=1}^M p(m|a^{(k-1)}) = \frac{d}{da^{(k-1)}} \sum_{m=1}^M 1 = 0. \end{aligned} \quad (A14)$$

As a consequence the partial derivatives of $G(S|A, \beta)$ with respect to A and β are equal to zero for $\{A=A^{(k-1)}, \beta=\beta^{(k-1)}\}$, which completes the proof.

To summarize the implications of the two properties: Property 1 guarantees that the goodness-of-fit improves with every iteration of EM. Property 2 implies that when the E-quantity can no longer be increased, we have converged to a local maximum of the goodness-of-fit.

Property 1 has an additional important implication: the M-step within EM does not have to be a true maximization, i.e. as long as the E-quantity is increased the goodness-of-fit will improve during the iteration. In the case of Gaussian basis functions (and some other basis functions as well) the M-step can be carried out exactly in closed form. For some other basis functions it may not be possible to perform the M-step analytically. According to Property 1, we can substitute for the maximization of the E-quantity a simpler procedure such as a steepest-ascent search.

APPENDIX B. APPLICATION TO SIMULTANEOUS DETECTION AND TRACKING

We now discuss the mathematical formulation of MLANS to the problem of concurrent detection and tracking of targets. Consider the problem of concurrently performing detection and tracking of multiple targets in the presence of heavy clutter returns. In this case MLANS estimates track parameters through a fuzzy association of returns in multiple frames into multiple classes of clutter and tracks. This novel approach to tracking results in a dramatic improvement of performance: the MLANS tracking exceeds the performance of existing tracking algorithms in terms of track initiation for multiple targets at low signal-to-clutter ratios.

Historically, intrinsic mathematical similarities between tracking and classification problems have not been explored. Tracking problems have been characterized by an overwhelming amount of data available from radar sensors. This has led to the development of suboptimal algorithms amenable to sequential implementation for handling high rate-data streams. Such algorithms based on Kalman filters converge to the optimal ML solution for single-object tracking; however, their generalization to multiple-object tracking has been difficult [9]. Classification and pattern recognition problems, on the other hand, have been characterized by an insufficient amount of data for unambiguous decisions, which has led to the development of Bayes classification algorithms, optimally utilizing all the available information.

Such optimal utilization of information is lacking in existing tracking algorithms. This leads to difficulties with tracking multiple objects in heavy clutter. As the number of clutter returns increases, it becomes increasingly difficult to initiate and to maintain tracks. A near optimal algorithm, Multiple Hypothesis Tracking [10] initiates tracks by considering all possible associations between multiple objects and clutter returns on multiple scans. This problem, however, is known to be non-polynomially complete [11]; that is, its optimal solution requires a combinatorially large amount of computation which is difficult to handle, even for neural networks, when the number of clutter returns is large. A partial solution to this problem is offered by the Joint Probability Density Association (JPDA) tracking algorithm [12], which performs fuzzy associations of objects and tracks, eliminating the combinatorial search. However, the JPDA algorithm performs associations only on the last frame using established tracks and is, therefore, unsuitable for track initiation.

The MLANS neural network explores mathematical similarity between tracking and classification problems and applies optimal Bayes methods to the problem of tracking multiple objects. By applying fuzzy classification to associating data in multiple scans and the ML estimation of clutter and track parameters, MLANS combines the advantages of both the MHT and the JPDA algorithmic approaches. In MLANS tracking, each track is a class characterized by the state parameters and by the track model. For example, tracks are characterized by their initial positions, velocities, and a trajectory model relating object coordinates over time to their current positions.

Consider first an initial simplified problem of tracking Doppler clutter characteristics in time at a fixed range and azimuth cell. Then the MLANS multimode Gaussian model given by Equation (9) in Section 2.2 of the main text must be modified to account for the continuous time dependence of the distribution parameters:

$$\begin{aligned}\bar{\omega}_m(t) &= \omega_{0m} + \omega_{1m} t + \frac{1}{2} \omega_{2m} t^2, \\ \Delta\omega_m(t) &= \Delta\omega_{0m} + \Delta\omega_{1m} t + \frac{1}{2} \Delta\omega_{2m} t^2, \text{ and} \\ A(t) &= A_{0m} + A_{1m} t + \frac{1}{2} A_{2m} t^2.\end{aligned}\tag{B1}$$

The likelihood must be modified by including the time index t into the sums in Equations (13) and (14) of Section 2.2 of the main text. Applying a procedure similar to that described for Equations (19) through (22), a set of equations is derived for the parameters

$$\omega_{0m}, \omega_{1m}, \omega_{2m}; \Delta\omega_{0m}, \Delta\omega_{1m}, \Delta\omega_{2m}; A_m, A_{1m}, A_{2m}.\tag{B2}$$

For the frequency parameters, we obtain the set of equations

$$\begin{aligned}0 &= \langle \omega \rangle - \omega_{0m} - \omega_{1m} \langle t \rangle - \frac{1}{2} \omega_{2m} \langle t^2 \rangle \\ 0 &= \langle \omega t \rangle - \omega_{0m} \langle t \rangle - \omega_{1m} \langle t^2 \rangle - \frac{1}{2} \omega_{2m} \langle t^3 \rangle \\ 0 &= \langle \omega t^2 \rangle - \omega_{0m} \langle t^2 \rangle - \omega_{1m} \langle t^3 \rangle - \frac{1}{2} \omega_{2m} \langle t^4 \rangle.\end{aligned}\tag{B3}$$

Here angular brackets $\langle \rangle$ are defined for a quantity, q , as weighted sums:

$$\langle q \rangle = \sum_{\omega, t} S(\omega, t) P(m|\omega, t) q.\tag{B4}$$

Equations (B3) are a linear system of equations for the parameters ω_{0m} , ω_{1m} , ω_{2m} and can be solved in a straight forward way at every MLANS iteration.

For the parameters of $\Delta\omega(t)$, similar procedures leads to

$$\begin{aligned} 0 &= \left\langle \Delta\omega_{0m} + \Delta\omega_{1m}t + \frac{1}{2}\Delta\omega_{2m}t^2 \right\rangle - \left\langle (\omega - \omega_m(t))^2 \frac{1}{\Delta\omega_m(t)} \right\rangle \\ 0 &= \left\langle \Delta\omega_{0m} + \Delta\omega_{1m}t + \frac{1}{2}\Delta\omega_{2m}t^2 \right\rangle t - \left\langle (\omega - \omega_m(t))^2 \frac{t}{\Delta\omega_m(t)} \right\rangle \\ 0 &= \left\langle \Delta\omega_{0m} + \Delta\omega_{1m}t + \frac{1}{2}\Delta\omega_{2m}t^2 \right\rangle t^2 - \left\langle (\omega - \omega_m(t))^2 \frac{t^2}{\Delta\omega_m(t)} \right\rangle \end{aligned} \quad (B5)$$

This is a nonlinear set of equations, which, however can be linearized by taking $\Delta\omega_m(t)$ in the denominator as the previous iteration values. This leads to a linear update system of equations for $\Delta\omega_{0m}$, $\Delta\omega_{1m}$, $\Delta\omega_{2m}$.

Similarly, a set of equations for the amplitude parameters is

$$\begin{aligned} 0 &= \left\langle \frac{1}{A_m(t)} \right\rangle + \lambda \sum_t 1 \\ 0 &= \left\langle \frac{t}{A_m(t)} \right\rangle + \lambda \sum_t t \\ 0 &= \left\langle \frac{t^2}{A_m(t)} \right\rangle + \lambda \sum_t t^2 . \end{aligned} \quad (B6)$$

This can be linearized by expanding $(A_m(t))^{-1}$ into a Taylor series, such that

$$\frac{1}{A_m(t)} = \frac{1}{A_0} \left[1 - \frac{A_1}{A_0} t - \left(\frac{A_2}{A_0} - \left(\frac{A_1}{A_0} \right)^2 \right) t^2 \right] . \quad (B7)$$

This leads to a linear system for

$$\frac{1}{A_0}, \frac{A_1}{A_0}, \left(\frac{A_2}{A_0} - \left(\frac{A_1}{A_0} \right)^2 \right) . \quad (B8)$$

An extension of this model to tracking in range R and azimuth θ requires different models for targets and clutter. We define a target model as a Gaussian radar ambiguity function around $R_m(t)$, $\theta_m(t)$, $\omega_m(t)$:

$$F(\omega, R, \theta | m) = G(\omega | \omega_m(t), \Delta\omega_m) G(R | R_m(t), \Delta R) G(\theta | \theta_m(t), \Delta\theta). \quad (B9)$$

A clutter model has a different shape: clutter exists at all R, θ with A_m, ω_m and $\Delta\omega_m$ being function of R, θ, t such that

$$\omega_m = \omega_m(R, \theta, t), \Delta\omega_m = \Delta\omega_m(R, \theta, t), A_m = A_m(R, \theta, t) \quad (B10)$$

This leads to a clutter model

$$F(\omega, R, \theta | m) = G(\omega | \omega_m(R, \theta, t), \Delta\omega_m(R, \theta, t)). \quad (B11)$$

A smooth spatial variability of the clutter model in space and time is parameterized by the following set of equations:

$$\begin{aligned} \omega_m(R, \theta, t) &= \omega_{0m} + \sum_i \omega_{1m}^i X_i + \frac{1}{2} \sum_{i,j} \omega_{2m}^{ij} X_i X_j \\ \Delta\omega_m(R, \theta, t) &= \Delta\omega_{0m} + \sum_i \Delta\omega_{1m}^i X_i + \frac{1}{2} \sum_{i,j} \Delta\omega_{2m}^{ij} X_i X_j \\ A_m(R, \theta, t) &= A_{0m} + \sum_i A_{1m}^i X_i + \frac{1}{2} \sum_{i,j} A_{2m}^{ij} X_i X_j \end{aligned} \quad (B12)$$

For the target model, the position of the target return in Doppler, range and azimuth can be modeled as

$$\omega_m(t) = \omega_{0m} + \omega_{1m} t + \frac{1}{2} \omega_{2m} t^2, \text{ and same for } R_m(t), \theta_m(t), A_m(t), \quad (B13)$$

while $\Delta\omega, \Delta R, \Delta\theta$ will be taken as constant over time and for different targets, being determined by the radar ambiguity function. The equations for these simultaneous detection and tracking parameters are derived using a procedure similar to that discussed for Equations (19) through (22) in Section 2.2 of the main text.

APPENDIX C. ASSESSMENT OF THE APPLICABILITY OF THE HYPERBOLIC FILTER TO HF RADAR TARGET DETECTION

The Hyperbolic Filter (known in the literature as the *fan filter* [13]) was originally devised to process image sequences for the purpose of enhancing moving targets with respect to clutter or noise. A task under the HF Propagation program was to assess the applicability of the Hyperbolic Filter to HF radar data.

Let $I(t,x,y)$ denote an image sequence, where I is the value of the image intensity, t is the index of the image (physically corresponding to time), and (x,y) are Cartesian coordinates within the image (i.e. pixel indices). The theory behind the Hyperbolic Filter assumes that the image sequence is a linear superposition of moving objects - both targets and clutter - in addition to uncorrelated noise. A particular moving object has the mathematical model

$$I(t,x,y) = a(x-v_x t, y-v_y t), \quad (C1)$$

and is characterized by $a(x,y)$, its image intensity distribution at the reference time $t=0$, and by an apparent velocity (v_x, v_y) , having units of pixels per frame. Both the image intensity distribution and the velocity are assumed constant with respect to time. The Hyperbolic Filter is a linear, shift-invariant filter having an impulse response $h(t,x,y)$. When applied to an image sequence $I(t,x,y)$, the output of the filter is an image sequence $\hat{I}(t,x,y)$ that is equivalent to the following 3-D convolution

$$\hat{I}(t,x,y) = \sum_{t'} \sum_{x'} \sum_{y'} h(t',x',y') \cdot I(t-t', x-x', y-y') \quad (C2)$$

In typical problems of clutter-limited target detection, the clutter occupies a continuous range of apparent velocity in the image sequence resulting from parallax. The unique property of the Hyperbolic Filter is that it rejects all moving objects over this continuous velocity set. Thus the operation of the Hyperbolic Filter is analogous to that of the familiar band-reject filter. By choosing the velocity cutoff set for the filter to coincide with the possible set of clutter velocities, the Hyperbolic Filter greatly increases the signal-to-clutter ratio for all targets having a velocity distinct from that of the clutter.

In order to apply the Hyperbolic Filter to HF radar data we need to have a signal that corresponds to the model (C1). The Doppler-filtered HF radar data can be denoted by power as a function of four variables $S(t, f_D, R, \theta)$, where t denotes time, f_D denotes Doppler frequency, R denotes range, and θ denotes azimuth. In general a moving target has two components of velocity: a radial component v_R and an azimuthal component v_θ that manifest themselves as progressive motion through range cells and azimuth cells, and as a peak in the Doppler spectrum at $f_D = -2v_r/\lambda$. Then a simplified signal model for a moving target, or for clutter, is

$$S(t, f_D, R, \theta) = F(f_D + 2v_r/\lambda) \cdot a(R - R_0 - v_R t) \cdot b(\theta - \theta_0 - v_\theta t), \quad (C3)$$

where $F(f_D)$ is the shape of the peak in the Doppler spectrum (e.g. a Gaussian curve), $a(R)$ is the shape of the compressed radar pulse, $b(\theta)$ is the beam pattern of the receiver antenna array, and (R_0, θ_0) is the position of the target at reference time $t=0$.

Comparing the two signal models given by Equations (C1) and (C3), it is apparent that the only way to apply the Hyperbolic Filter to HF radar data would be to apply the filter to the Doppler-filtered data, for a particular value of Doppler frequency, i.e., to fix f_D and to treat the data as a function of (t, R, θ) . However, the Doppler filtering will already have suppressed all targets and clutter having a radial velocity significantly different than the radial velocity associated with the particular Doppler frequency.

The principle obstacle to realizing any significant advantages with the Hyperbolic Filter is the vastly greater motion sensitivity of Doppler filtering compared with motion through range and azimuth cells. Consider some typical radar parameters: radar operating frequency = 25.68 MHz, coherent integration time = 2.1333 s, range resolution = 8.1 nm (15 km), azimuth resolution = 2.5 degrees, range = 1542 nm (2856 km). The corresponding Doppler resolution is 0.469 Hz, which is equivalent to a radial velocity resolution at the given operating frequency of 2.74 m/s. In contrast, over a twelve-minute (720 s) tracking time (the stipulated mean tracking time with 15 dB SNR), the radial velocity resolution due to target motion through range cells is $15000/720$ or 20.8 m/s. At a range of 1542 nm, the 2.5 degree azimuth resolution is equivalent to a cross-range resolution of 125 km, so over a twelve-minute tracking time the azimuthal velocity resolution is only 173 m/s. In short, unless the target is moving exactly perpendicular to the line-of-sight (in which case it is not a threatening target) then motion through azimuth cells is of no help. In turn, if

the radial velocities of the target and clutter are sufficiently different so that differential movement through range cells can be observed, the same effect will be observed and exploited with much greater sensitivity in the Doppler spectrum. In short, there does not seem to be any regime where it would be advantageous to use the Hyperbolic Filter.

MISSION OF ROME LABORATORY

Mission. The mission of Rome Laboratory is to advance the science and technologies of command, control, communications and intelligence and to transition them into systems to meet customer needs. To achieve this, Rome Lab:

- a. Conducts vigorous research, development and test programs in all applicable technologies;
- b. Transitions technology to current and future systems to improve operational capability, readiness, and supportability;
- c. Provides a full range of technical support to Air Force Material Command product centers and other Air Force organizations;
- d. Promotes transfer of technology to the private sector;
- e. Maintains leading edge technological expertise in the areas of surveillance, communications, command and control, intelligence, reliability science, electro-magnetic technology, photonics, signal processing, and computational science.

The thrust areas of technical competence include: Surveillance, Communications, Command and Control, Intelligence, Signal Processing, Computer Science and Technology, Electromagnetic Technology, Photonics and Reliability Sciences.